Computational Icing Risk Analysis of the D8 "Double Bubble" Aircraft

Christopher E. Porter and Mark G. Potapczuk
Glenn Research Center, Cleveland, Ohio

NASA STI Program . . . in Profile

Since its founding, NASA has been dedicated to the advancement of aeronautics and space science. The NASA Scientific and Technical Information (STI) Program plays a key part in helping NASA maintain this important role.

The NASA STI Program operates under the auspices of the Agency Chief Information Officer. It collects, organizes, provides for archiving, and disseminates NASA's STI. The NASA STI Program provides access to the NASA Technical Report Server—Registered (NTRS Reg) and NASA Technical Report Server—Public (NTRS) thus providing one of the largest collections of aeronautical and space science STI in the world. Results are published in both non-NASA channels and by NASA in the NASA STI Report Series, which includes the following report types:

- TECHNICAL PUBLICATION. Reports of completed research or a major significant phase of research that present the results of NASA programs and include extensive data or theoretical analysis. Includes compilations of significant scientific and technical data and information deemed to be of continuing reference value. NASA counter-part of peer-reviewed formal professional papers, but has less stringent limitations on manuscript length and extent of graphic presentations.

- TECHNICAL MEMORANDUM. Scientific and technical findings that are preliminary or of specialized interest, e.g., "quick-release" reports, working papers, and bibliographies that contain minimal annotation. Does not contain extensive analysis.

- CONTRACTOR REPORT. Scientific and technical findings by NASA-sponsored contractors and grantees.

- CONFERENCE PUBLICATION. Collected papers from scientific and technical conferences, symposia, seminars, or other meetings sponsored or co-sponsored by NASA.

- SPECIAL PUBLICATION. Scientific, technical, or historical information from NASA programs, projects, and missions, often concerned with subjects having substantial public interest.

- TECHNICAL TRANSLATION. English-language translations of foreign scientific and technical material pertinent to NASA's mission.

For more information about the NASA STI program, see the following:

- Access the NASA STI program home page at http://www.sti.nasa.gov

- E-mail your question to help@sti.nasa.gov

- Fax your question to the NASA STI Information Desk at 757-864-6500

- Telephone the NASA STI Information Desk at 757-864-9658

- Write to:
  NASA STI Program
  Mail Stop 148
  NASA Langley Research Center
  Hampton, VA 23681-2199

Computational Icing Risk Analysis of the D8 "Double Bubble" Aircraft

Christopher E. Porter and Mark G. Potapczuk
Glenn Research Center, Cleveland, Ohio

National Aeronautics and
Space Administration

Glenn Research Center
Cleveland, Ohio 44135

Acknowledgments

Level of Review: This material has been technically reviewed by technical management.

Available from

Computational Icing Risk Analysis of the
D8 "Double Bubble" Aircraft

Christopher E. Porter and Mark G. Potapczuk
National Aeronautics and Space Administration
Glenn Research Center
Cleveland, Ohio 44135

Abstract

A computational icing risk analysis utilizing LEWICE3D was performed for the D8 Double Bubble aircraft. A variety of discrete drop sizes spanning the Appendix C and O regimes were simulated. For computational efficiency a 50-bin global discretization was produced and projected onto the distributions of interest, eliminating redundant simulations. The trajectory and impingement characteristics for discrete drop diameters were analyzed to help understand the behavior of the water drops in the presence of a complex flow field. The collection efficiency results for the discrete drop diameters were then weighted by their contributions to the total water content of six different continuous distributions and subsequently superposed to approximate these curves. Results indicate that significant variation in impingement exists as a function of drop diameter for complex wing body geometries, and that current discretization practices may be insufficient to accurately predict water collection on certain regions of the aircraft. Results also indicate that the Appendix O distributions, specifically those with considerable water content at large drops, generates water collection patterns that are markedly different from distributions representative of Appendix C.

Nomenclature

AoA	Angle of Attack
β (beta)	Local Collection Efficiency
CFD	Computational Fluid Dynamics
d_i	Discrete Droplet Diameter
FAA	Federal Aviation Administration
LWC	Liquid Water Content
M_∞	Freestream Mach Number
MIT	Massachusetts Institute of Technology
MVD	Median Volume Diameter
NASA	National Aeronautics and Space Administration
Re_∞	Free Stream Reynolds Number
SLD	Supercooled Large Drops
SST	Shear Stress Transport (Turbulence Model)
TWC	Total Water Content
μm	micron/micrometer
V_∞	Free Stream Velocity

Introduction

The Advanced Air Transport Technology project of the Advanced Air Vehicles Program under the Aeronautics Research Mission Directorate at NASA has an ongoing interest in developing revolutionary next generation (N+3) commercial transport designs that are energy efficient and environmentally compatible (Ref. 1). To achieve these goals the N+3 aircraft employ designs that are atypical of current commercial transport vehicles. These atypical designs include high aspect ratio and truss braced wings, lifting fuselages, boundary layer ingesting engines, and blended wing bodies. These design features can be seen in the five N+3 geometries depicted in Figure 1.

There are three primary ways to investigate the icing risk of airframe geometries: (1) flight testing, (2) icing tunnel testing, and (3) computational simulation. Flight testing offers the best results, as the full scale aircraft can be flown through realistic conditions. However, this requires a full scale aircraft to be designed and built as well as seeking transient icing weather conditions as they occur in nature. Due to the cost associated with these steps, this method is not necessarily desirable for the evaluation of aircraft that are in the early design stages of development.

Icing tunnel testing attempts to simulate flight testing. It has advantages over flight testing, such as providing the user control over the operating condition and repeatability. However, tunnel testing restricts model size to some fraction of the test section size of the tunnel in which it is being tested. Due to scaling complexities associated with the icing phenomenon, generating a representative scaled geometry and test matrix is both time consuming and costly.

Computational icing tools attempt to replicate both of the above. However, the icing problem is an unsteady, turbulent, multiscale, and multiphase phenomenon. Simulating all of the physical effects that contribute to airframe icing with currently available computational resources is not feasible. Therefore, these computational icing tools only attempt to capture the first order, or dominant, effects so that simulations can be computed in time frames conducive for research and development, while still providing a reasonable solution. Because these tools only approximate the water impingement of a droplet distribution, as well as the resulting ice shape, the tools must be sufficiently validated to be used in a predictive fashion.

LEWICE3D (Ref. 2) is a quasi-3D ice accretion solver, and for straight wings, is nearly indistinguishable from LEWICE, a two-dimensional ice accretion solver that is considered a validated production level code (Ref. 3) with respect to the Title 14 CFR Part 25 Appendix C (Ref. 4) regime. Due to the degrees of freedom a third dimension adds to the problem, as well as the Supercooled Large Drops found in Title 14 CFR Part 25 Appendix O (Ref. 5), there are aspects of LEWICE3D that aren't

Figure 1.—Five Various N+3 Geometries. Top (Left to Right): D8 "Double Bubble", HWB, SUGAR VOLT – Bottom (Left to Right): STARC-ABL, N3X.

sufficiently validated. However, there is still usefulness in LEWICE3D analyses even outside the validated predictive range. It provides a cost-effective insight into a complex problem. For instance, LEWICE3D has been used in the past to assess wing-only (Refs. 6 and 7), engine inlet (Ref. 8), as well as classical wing body configurations (Refs. 7, 9, and 10).

One of the complexities that can arise is the splashing problem. It has been shown that the splashing of large drops can attribute to reduced collection efficiency in the regions aft of the stagnation point (Ref. 7). The same study illustrated that the splashing model in LEWICE3D v.3 provided collection efficiency results that agreed more favorably with experiment than LEWICE3D results without the splashing model.

Another complexity that can arise is the influence upstream geometries have on downstream collection efficiencies. A simulation of the NASA S3 aircraft (Ref. 10) suggests that the upstream geometry "hides" the downstream surfaces from water impingement, generating what the author called a shadowzone. At the edges of these shadowzones are regions of high collection efficiency where "a concentrating effect or compression effect on the particles, similar to streamlines traversing the leading edge region of a wing" occur. It was noted that this phenomenon primarily affects the larger dropsizes in the distributions.

LEWICE3D is a tool that has historically provided reasonable insight into regions of the aircraft that may be susceptible to unique and/or significant icing risk, even those outside of its range of validation.

This paper discusses the details of the D8 geometry, the computational tools used, and the operating conditions simulated in an effort to identify regions of icing risk for the D8 aircraft using LEWICE3D. The metric used here to define icing risk is the water collection characteristics of the components, or local collection efficiency. This definition was favored for a variety of reasons: (1) the amount of water collecting on the surface correlates to the size and potential performance impact of the accreted ice in that region as well correlating with the requirements for anti-icing components needed to protect these regions, (2) a level of confidence exists in the fully 3D trajectory routine in steady flow fields, (3) there is an unknown confidence in the quasi-3D ice growth module on unvalidated surfaces, and (4) inclusion of ice shape comparisons and the resulting aerodynamic degradation for multiple thermal operating points would increase the scope of the paper considerably. Subsequently, the computation of ice shapes is considered outside the scope of this particular paper.

Geometry and Simulation Details

Geometry

The geometry being assessed in this paper is the D8 "Double Bubble" aircraft (Ref. 11). Its design is the result of a NASA sponsored joint effort between Aurora Flight Sciences, MIT and Pratt & Whitney. There are multiple variants of the D8 design. The design provided for this effort, pictured in Figures 1 and 2, consisted of a two engine configuration rather than the three engine configuration seen in previous mock-ups. This design has a half-span of 75 ft (900 in.), a body length of 114.9 ft (1379 in.) and a mean chord length of 10 ft (120 in.).

Simulation

Operating Condition, Mesh, and CFD Solver Details

The flight operating condition simulated is one that is representative of a typical hold pattern for commercial aircraft. The hold pattern is the portion of the flight where the aircraft is exposed to icing conditions for extended periods of time. It should be noted that this representative hold condition is almost assuredly not the *exact* hold condition for this particular aircraft. Determining that specific hold condition would have required additional aerodynamic analysis. The purpose of this study is to assess the icing risks for the D8 aircraft. Thus, utilization of a representative operating condition, and not necessarily the exact operating condition, was deemed sufficient to meet that goal. Details of the simulated flight condition are listed in Table 1.
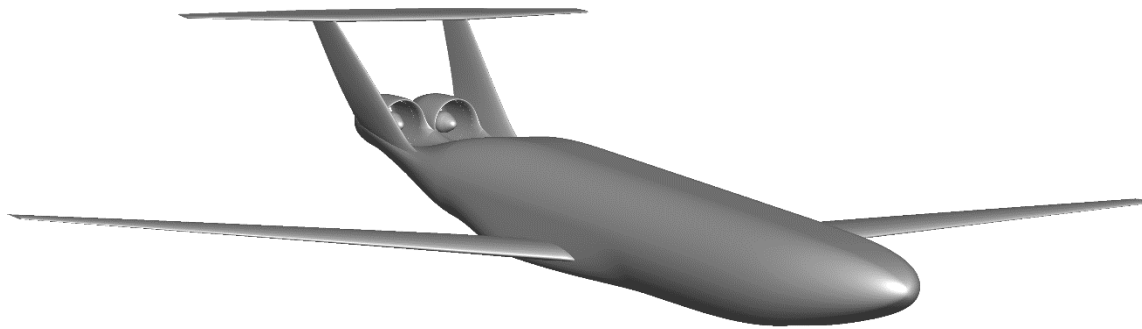
Figure 2.—D8 "Double Bubble" Computational Surface Geometry.

TABLE 1.—SIMULATED OPERATING CONDITION FOR THE D8 "DOUBLE BUBBLE"

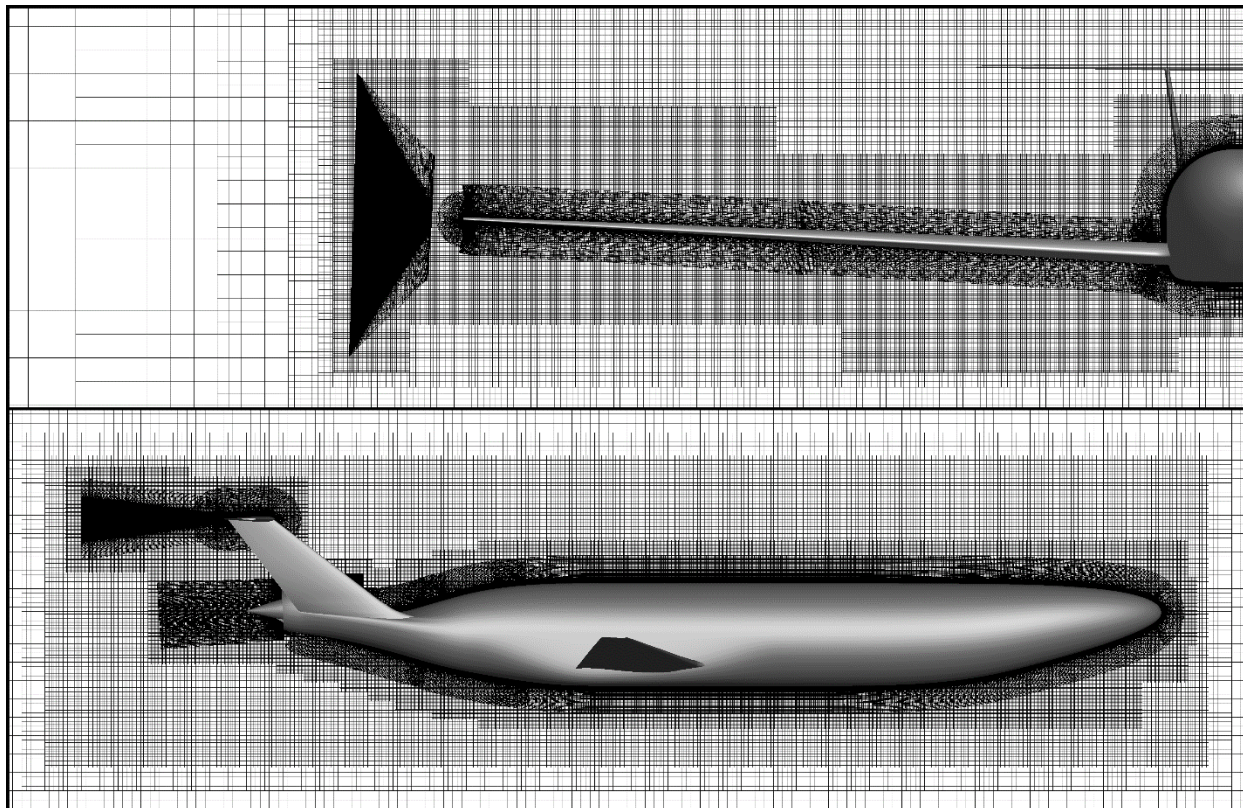| V_∞, mph	Altitude, ft	AoA, degree	M_∞	Re_∞
200	10,000	4	0.272	14,511,360

Figure 3.—X-plane and Y-plane Cuts of the Near Body Overset Mesh.

The mesh contained 423 overset blocks, with each block consisting of a structured mesh with hexahedral cells. The number of grid points in the entire mesh was on the order of 288 million. The domain boundaries were placed well in the freestream, roughly 50 body lengths away from the aircraft. A first cell height of y+≈1 was targeted, and achieved on most the body surfaces. Y+ is a nondimensional quantity that describes the boundary layer, with values of 1 considered to be resolved. X-plane and Y-plane cuts of the near body overset mesh are shown in Figure 3.
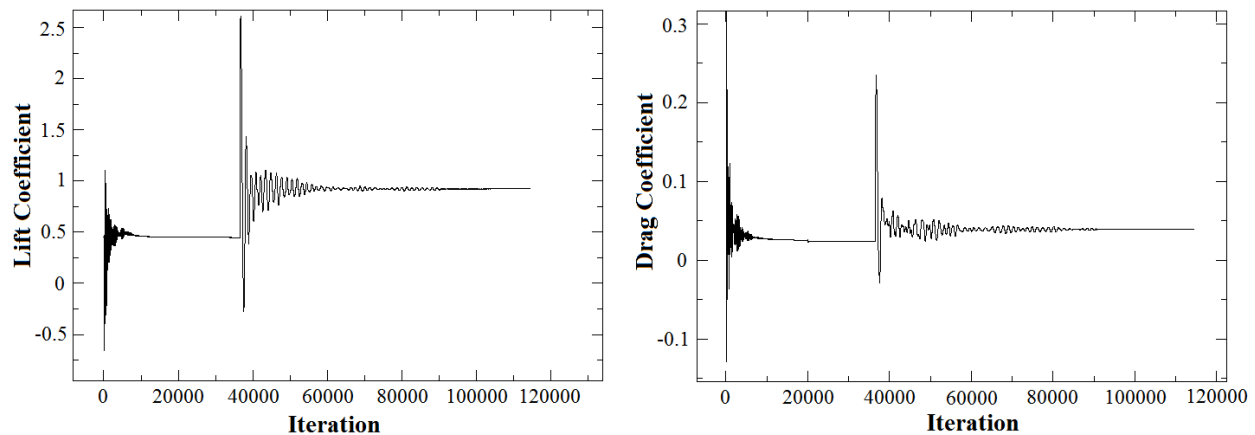
Figure 4.—Lift Coefficient and Drag Coefficient Convergence Histories.

The flow simulations were completed by H. Doğuş Akaydin and Shishir Pandya at NASA Ames Research Center. The CFD solver utilized was the in-house NASA solver, Overflow, version 2.2k (Ref. 12). It is a Reynolds Averaged Navier Stokes solver with a variety of flux and turbulence schemes. A 2nd order central finite difference scheme was employed, along with the SST turbulence model. The SST turbulence model is a blended model that utilizes a k-ω scheme in the near wall region, a k-ε scheme in the free shear region, and a blending function to smoothly transition between the two (Ref. 13). The lift coefficient and drag coefficient histories are shown in Figure 4, and illustrate that some level of convergence was achieved on the finest multigrid level.

LEWICE3D Details

LEWICE3D version 3.63 was used for this analysis. LEWICE3D is a CFD post processor that utilizes the computed steady-state q-vector to calculate Lagrangian particle trajectories through the flow field. It should be noted, however, that this Lagrangian method isn't tracking individual drops. Instead, each computed trajectory represents a stream tube of a small finite area. The collection efficiency is then computed as the freestream area of the impacting stream tubes divided by the area of the surface cell. This method requires a sufficiently resolved stream tube discretization to ensure numerical accuracy. In order to achieve the required refinement, LEWICE3D employs an octree approach to self-resolve the trajectory field. By framing the problem in this fashion, computational time is greatly reduced.

In order to compute continuous droplet distributions, the distribution is discretized into bins with each bin having a representative discrete dropsize, typically the MVD of that bin. Each bin is simulated independently by computing the impingement characteristics of the representative droplet size. The resulting collection efficiencies of all of the bins are superposed in a weighted fashion. The weighting function is equal to the fractional amount of the TWC each bin contributes to the distribution.

It should be noted that these simulations were run absent of the splashing model. While the splashing model has the potential to be more accurate, comparisons in Reference 7 were made on wing-only sections with a 92 μm distribution. Only 5 percent of the LWC was greater than 200 μm and contained a maximum drop size of roughly 400 μm. The effect of splashing with respect to dropsizes over 400 μm, blunt bodies such as the fuselage, or bodies containing downstream geometries were not investigated. Thus, while the splashing model agrees very favorably for the simple wing-only geometries tested at moderate dropsizes, it is unclear how it would behave on complex geometries in the presence of extremely large dropsizes. Reference 7 also illustrated that the lack of a splashing model produced more conservative results. Since the purpose of this study is to identify potential icing risk, it is natural to favor a well understood model that produces conservative results.

LEWICE3D also computes the mass and energy balance of the surface water that enables the prediction of ice shapes for various thermal operating conditions. However, this paper is focused on the water impingement characteristics of various dropsizes/clouds. As such, a detailed description of this process is not relevant for this paper. However, if the reader is interested in these modules and algorithms, more information can be found in the LEWICE3D Users Manual (Ref. 2).

Droplet Distributions

Six distributions were chosen for this study. The first two distributions are 20 and 40 μm MVD distributions. These distributions are representative of the Title 14 CFR Part 25 Appendix C (Ref. 4) Continuous Maximum (Stratiform Clouds) and Intermittent Maximum (Cumuliform Clouds) icing conditions, respectively. The distributions themselves are Langmuir "D", (Ref. 14) which is a commonly used distribution for Appendix C conditions (Ref. 15). It should be noted that the Langmuir "D" distribution is a discretized distribution and numerically documented by its 7-bin representation. However, a higher resolution of the Langmuir "D" curve is desired for the purposes of this paper. Reference 16 depicts a figure of the discretized Langmuir "D" distribution along with a continuous representation of the distribution. It is not clear where the continuous distribution originated or how it is calculated. However, a cubic spline representation of the 7-bin Langmuir "D" distribution, along with the implied boundary condition at d_i/MVD = 0 and an assumed boundary condition at d_i/MVD = 3, produced a continuous curve that was visually identical to that depicted graphically in Reference 16. This high resolution, cubic spline representation of the Langmuir "D" distribution was used to generate the higher sampled discrete distributions seen in this paper. The nine data points used for the cubic spline are listed in Table 2. Note that the cumulative mass tabulated here is an increasing function rather than the decreasing function depicted in Reference 16. This was done to maintain consistency with Title 14 CFR Part 25 Appendix O (Ref. 5) where the distributions are depicted as increasing functions.

The other four distributions are graphically documented in Appendix O (Ref. 5). They are the "Freezing Drizzle MVD Less than 40 μm", "Freezing Drizzle MVD Greater than 40 μm", "Freezing Rain MVD Less than 40 μm", and the "Freezing Rain MVD Greater than 40 μm" distributions. Highly resolved (1 μ increment) numerical representations of these distributions were obtained from the FAA William J. Hughes Technical Center.

Discretization of the Droplet Distributions

The distributions being simulated in this document consist of drop diameter ranges that span three orders of magnitude. The array of drop diameters chosen to discretize these ranges is a 50-bin integer approximation of a 12.5 percent growth curve with an initial droplet diameter of 5 μm. The formula for this distribution can be seen in Equation (1) where d represents the droplet diameter in microns and i represents the bin index.

$$d_i = \left\lceil 5\left(1.125\right)^{(i-1)} \right\rceil \tag{1}$$

For clarity, please note that the $\lceil \ \rceil$ symbols represent the ceiling function, which maps the argument to the least integer greater than or equal to the argument, i.e., it rounds the argument up.

Portions of both the exact and rounded growth distributions can be seen in Table 3 with the resulting drop diameters illustrated graphically in Figure 5. Note the slight "hump" in the data at lower drop diameters (< 20 μm) that is most visible on the logarithmic plot in Figure 5. This is an artifact of the integer rounding being more significant in relative magnitude at the lower drop diameters. At the higher drop diameters, where this rounding is less significant in relative magnitude, the integer based discretization more closely approximates the exact 12.5 percent growth curve.

TABLE 2.—THE NINE DATA POINTS USED TO GENERATE THE CUBIC SPLINE CONTINUOUS LANGMUIR "D" CURVE

d_i/MVD	0.000	0.310	0.520	0.710	1.000	1.370	1.740	2.220	3.000
Cumulative mass	0.000	0.025	0.100	0.250	0.500	0.750	0.900	0.975	1.000

TABLE 3.—50-BIN DISCRETE DROPLET DISTRIBUTION. BOTH THE EXACT 12.5 PERCENT GROWTH ARRAY
(2nd COLUMN) AND ITSINTEGER APPROXIMATION (3rd COLUMN) ARE PICTURED

Bin index	Droplet diameter, µm	Droplet diameter, µm
1	5	5
2	5.625	6
3	6.328125	7
⋮	⋮	⋮
48	1268.056368	1269
49	1426.563414	1427
50	1604.883841	1605

Droplet Diamter vs. Bin Index
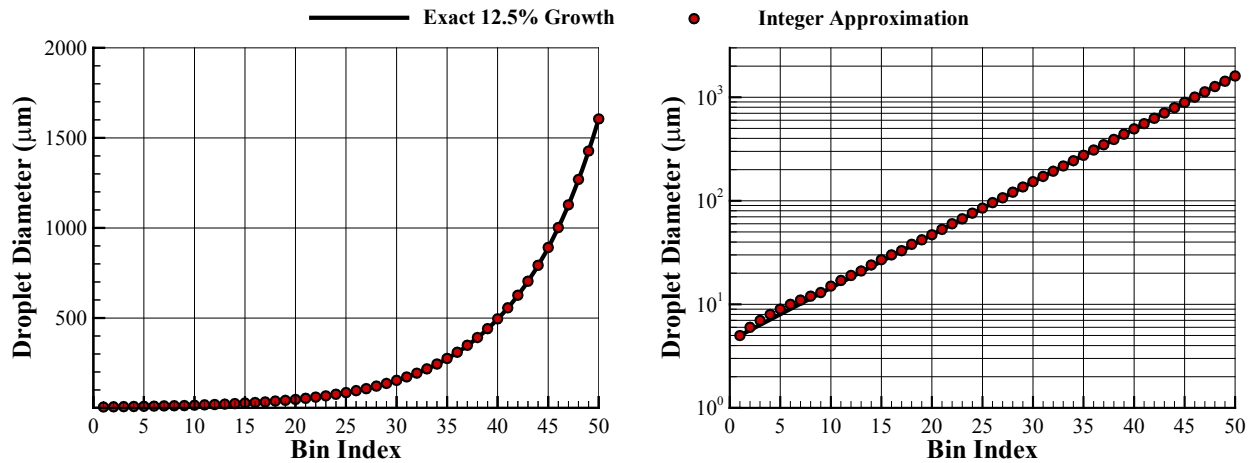
Figure 5.—50-Bin Discrete Droplet Distribution. Left: Linear Y-Axis. – Right: Logarithmic Y-Axis.

The graphs in the left column of Figures 6 and 7 illustrate the projection of the 50-bin discretization shown in Figure 5 onto the six desired droplet distributions. The graphs in the right column of Figures 6 and 7 illustrate the fractional TWC contained in each bin. These fractions are the weights used in the super position algorithm of LEWICE3D.
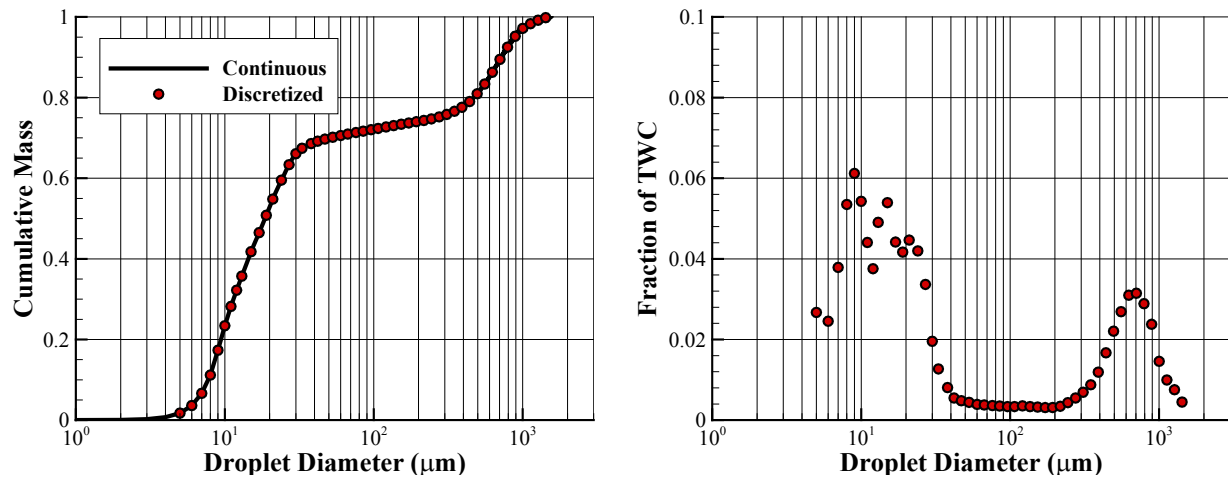
Langmuir "D" (20 μm) [High Resolution - Cubic Spline Interpolated]

Langmuir "D" (40 μm) [High Resolution - Cubic Spline Interpolated]

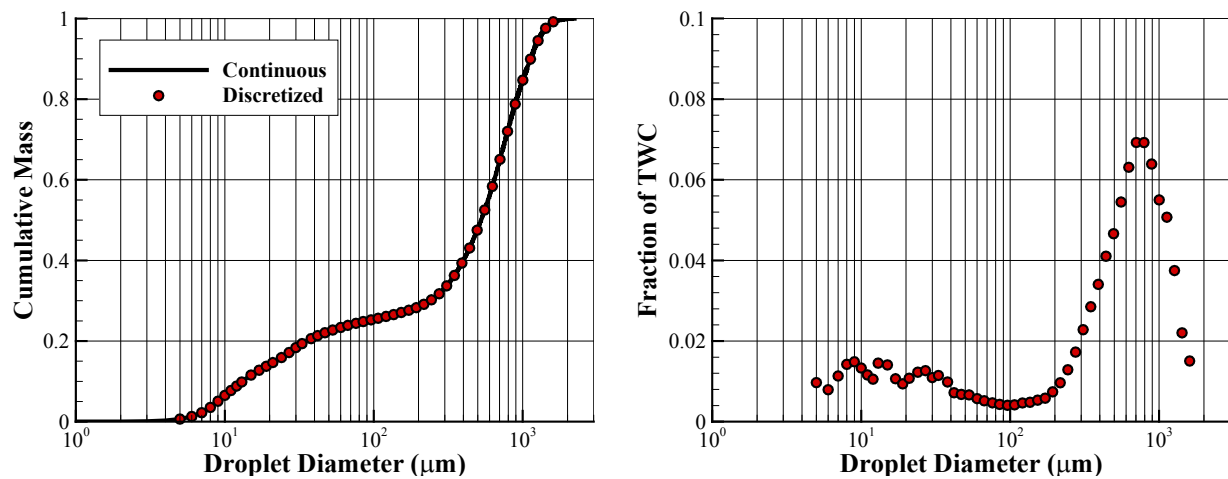# Freezing Drizzle MVD Less than 40 μm
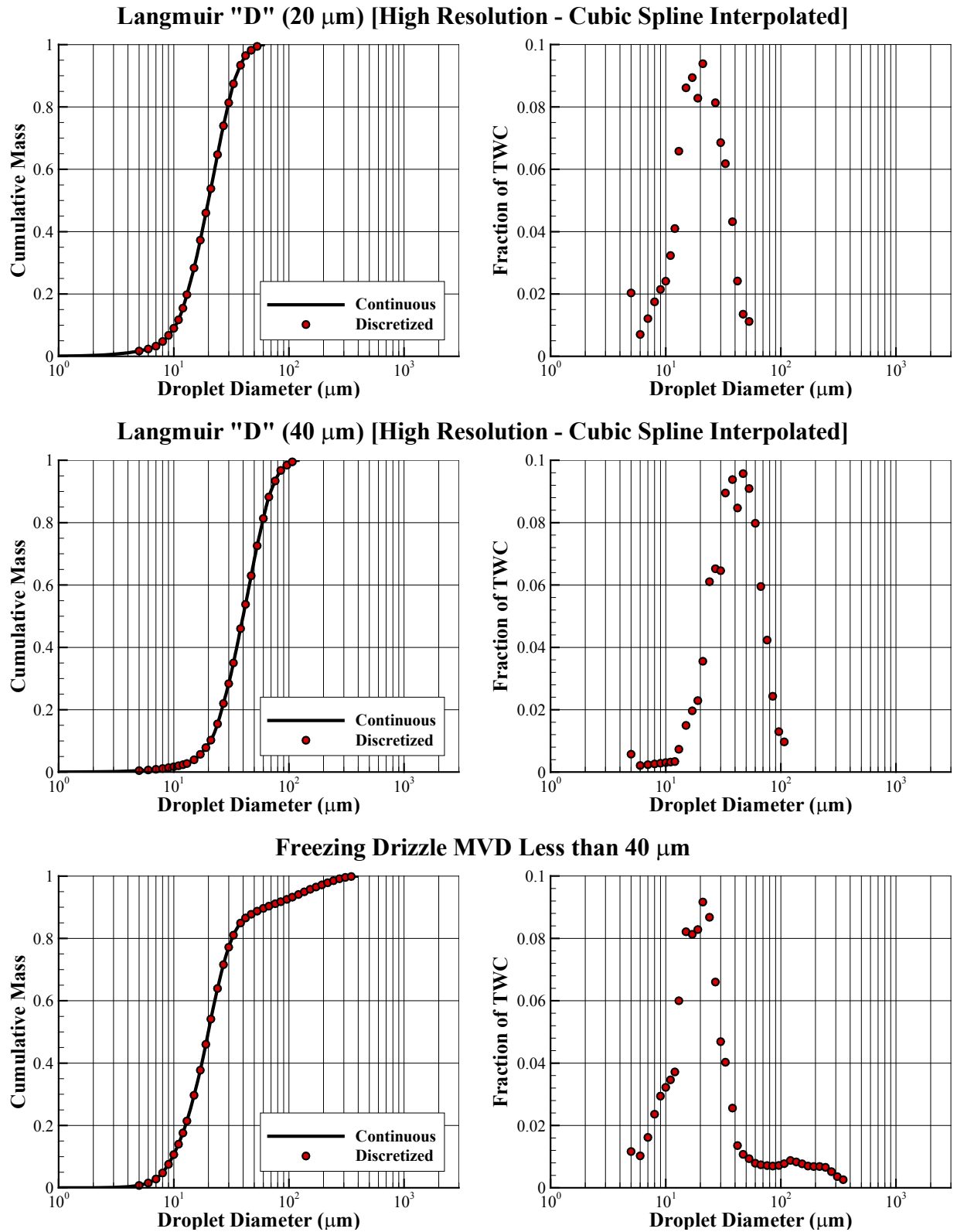
Figure 6.—50-Bin Representations of Various Drop Diameter Distributions. Left: Discretization of the Continuous Distributions. – Right: Amount of Total Water Content in Each Bin.
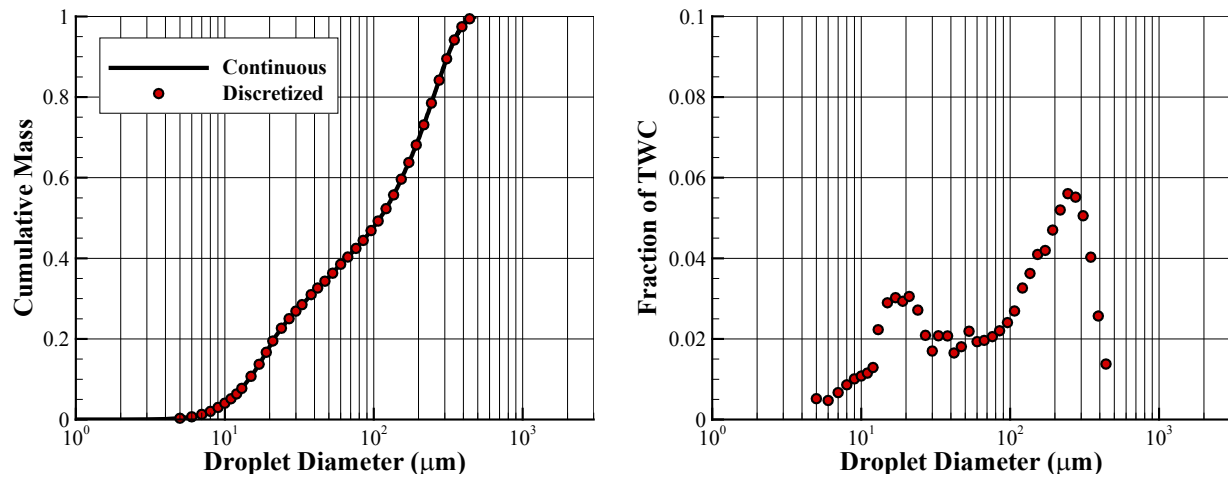
Figure 7.—50-Bin Representations of Various Drop Diameter Distributions. Left: Discretization of the Continuous Distributions. – Right: Amount of Total Water Content in Each Bin.

Results and Discussion

This section examines surface contours of collection efficiency (beta) for the D8 "Double Bubble" aircraft. This parameter was chosen as an icing risk metric since the water loading correlates with the size of the accreted ice and potential performance impact, as well as the sizing and requirements of the necessary ice protection system to mitigate the icing threat. Therefore, regions of high collection efficiency, as well as large surface areas of water loading are deemed to be an icing risk.

The first portion of the results examines a subset of discrete drop diameters to illustrate the difference in impingement characteristics due to droplet size. The second portion examines the droplet distribution results that were calculated by superpositioning weighted discrete droplet results. Only pertinent contours are pictured in this section. For a more comprehensive set of surface contours, the reader is directed to the appendix at the end of this paper.

Discrete Drop Sizes

Bin 1 (5 μm)

On the surface the results from Bin 1, a 5 μm case pictured in Figure 8, look rather uninteresting. These small drops are so light and have such low momentum that they follow the flow quite well and rarely impinge the aircraft posing no icing risk. However, this result is still very important. As can be seen in Figures 6 and 7, especially in the "Freezing Rain MVD Less than 40 μm" distribution, significant portions of the cloud's total water content can be attributed to small drop diameters. Thus, these small drop diameters must be properly represented in the simulation to avoid an over prediction of water collection that may occur with a coarser bin discretization.

Bin 17 (33 μm)

Figure 9 illustrates the impingement of 33 μm diameter drops. Notice that the increase in mass of the drops, and by extension momentum, allows the particles to be more ballistic in nature resulting in a significant increase in impingement. The upper portion of the engine cowling sees the most local water collection with leading edge collection efficiencies near unity, posing a significant icing risk on this component. A concentration effect is observed on the engine cowling in the regions neighboring the shadow zones where the collection efficiencies exceed unity. The cause of this effect is illustrated in Figure 10 which depicts trajectories on the symmetry (XZ) plane released upstream of the aircraft with a constant Z spacing. Notice that the trajectories closest to the stagnation point have the most curvature due to their presence in regions of higher velocity gradient. This effect causes these trajectories to migrate away from the body more rapidly than their neighboring trajectories. However, because the neighboring trajectories were further away from the body to begin with, the trajectories coalesce generating these regions of high local water content next to the shadowzones which significantly impacts the water impingement on the downstream geometries in these regions of the flowfield.
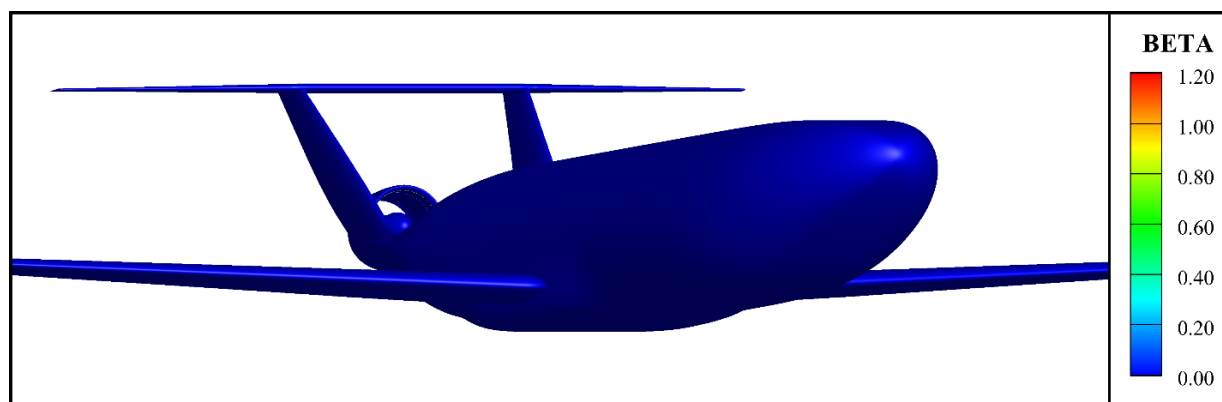

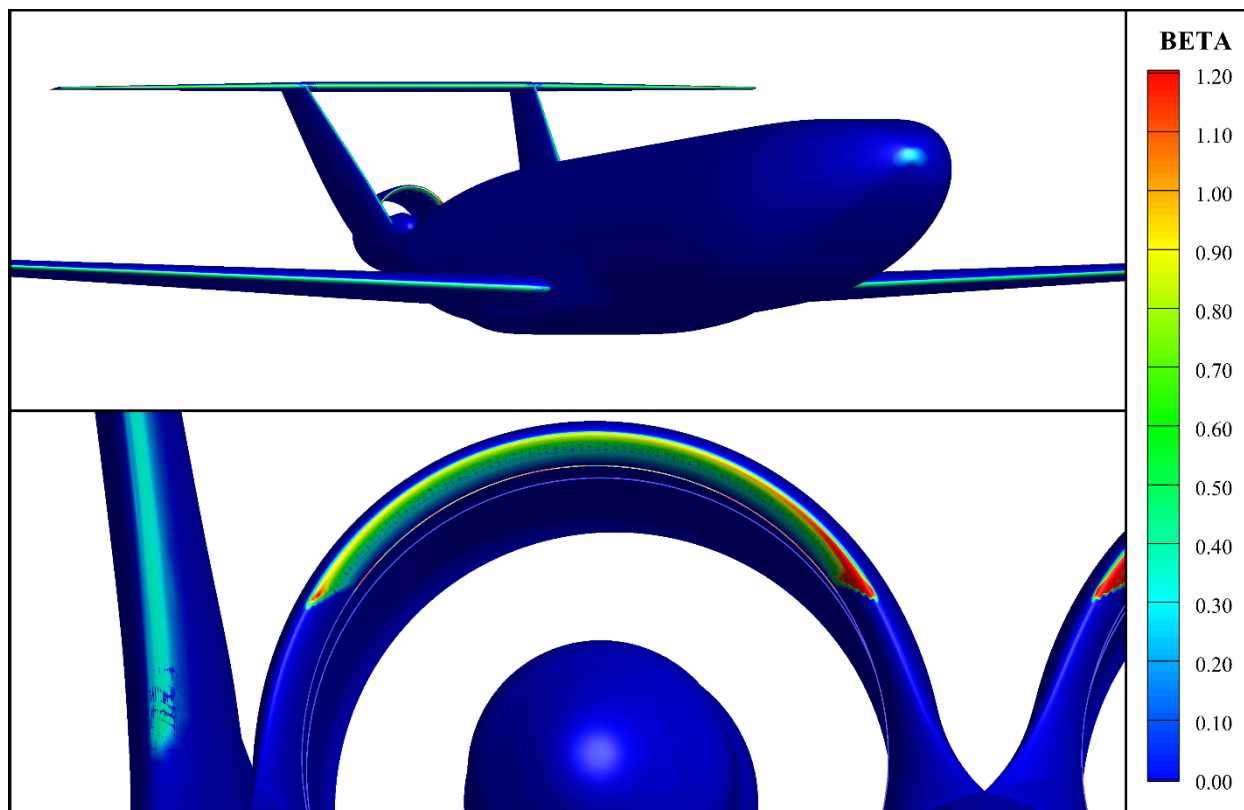Figure 8.—Collections Efficiencies for Bin 1, a Discrete Drop Diameter of 5 μm.

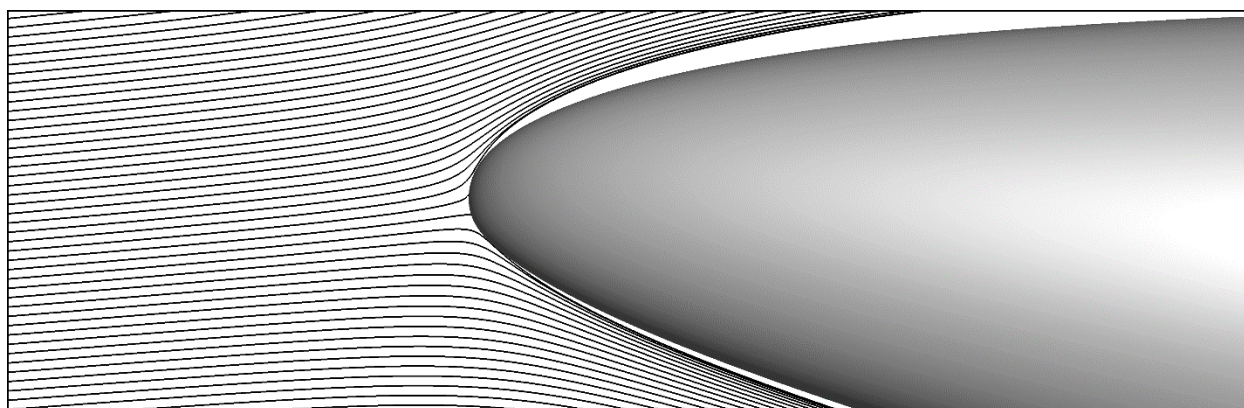Figure 9.—Collection Efficiencies for Bin 17, a Discrete Drop Diameter of 33 µm.

Figure 10.—Trajectories of 33 µm Drops Around the Nose of the D8 Aircraft.

Bin 34 (244 µm)

The increase in drop diameter to 244 µm again forces the particles to be even more ballistic in nature generating collection efficiencies of unity or higher on the nose, wings, and tails with impingement limits extending far back on these surfaces. This large drop size poses a significant icing threat on these components. This ballistic nature also increases the extent of the shadowzones aft of the nose. Figure 11 illustrates that the shadowzone at the root of the wing has become more pronounced, with a concentration effect forming in this region as well. The shadowzone above the fuselage near the tail has grown to such an extent that the engine cowling is now entirely in the shadowzone region and therefore does not pose an icing risk. From this result it can be inferred that only a limited number of small drop diameters collect on the engine cowling.

Comprehensive analysis of all the simulated drop diameters illustrate that the maximum drop diameter that impinges on the engine cowling is 47 µm. The collection efficiency contour of the engine cowling for the 47 µm case is pictured in Figure 12 highlighting that only a tiny portion of the upper cowling is impacted for this case. While the upper bound on this contour plot remains at 1.2 for consistency and readability, this thin region is characterized by an extremely high collection efficiency, with local collection efficiencies reaching values as high as 15. While this is a concentration region, the extremely large collection efficiency is likely due to the idealized nature of both the steady flow simulation and the cloud, and not necessarily a result that would be seen in an actual icing encounter.
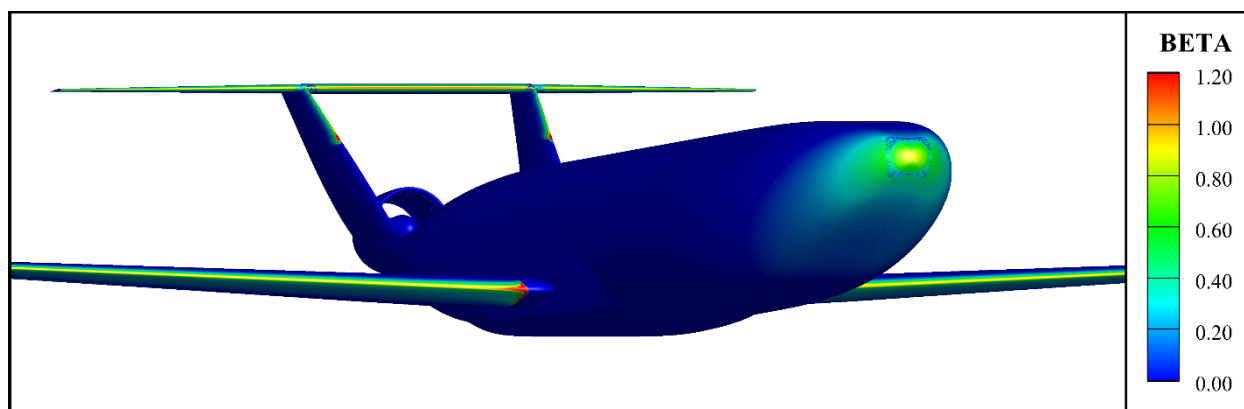

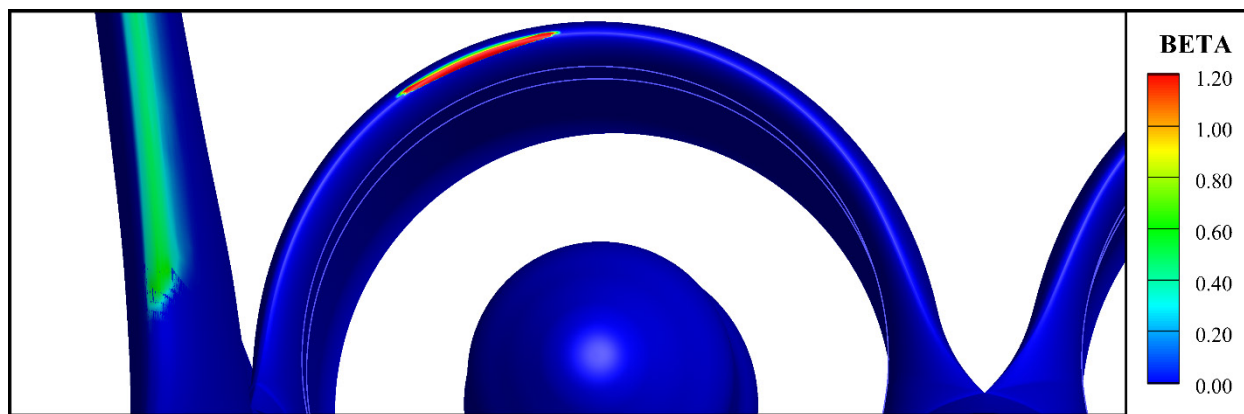Figure 11.—Collection Efficiencies for Bin 34, a Discrete Drop Diameter of 244 µm.

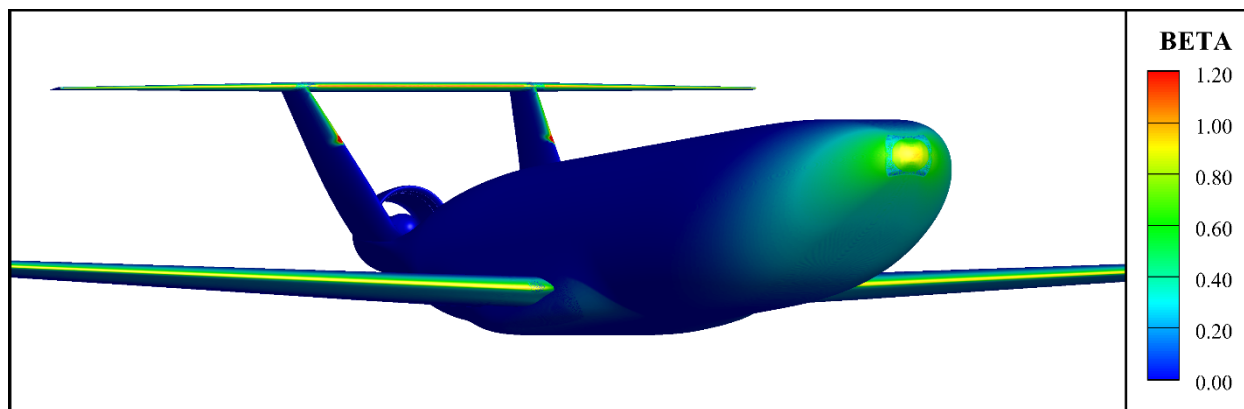Figure 12.—Collection Efficiencies on the Engine Cowling for Bin 20, a Discrete Drop Diameter of 47 µm.

Figure 13.—Collection Efficiencies for Bin 50, a Discrete Drop Diameter of 1605 μm.

Bin 50 (1605 μm)

The largest drop diameter simulated reveals some interesting phenomenon. In Figure 13 it is visually apparent that the shadowzone at the root of the wing has vanished. In its place is a collection efficiency trend that extends all the way to where the wing meets the fuselage. There is also a region of the fuselage just forward of the leading edge of the wing that water drops impinge upon. This result suggests that the drops are so ballistic in nature that velocity gradients in the flow field have a reduced effect on the droplet trajectories.

The shadowzone on the vertical tail remains highlighting that this shadowzone and the one at the wing root are slightly different. The shadowzone at the wing root is generated solely by the velocity gradients. That is to say the wing root is in the line of sight of the upstream drops, therefore trajectories that are purely ballistic in nature will impinge. Due to the 4° angle of attack of the aircraft, the engine cowlings and portions of the vertical tail are not in the line of sight of upstream trajectories. Thus drops that are purely ballistic are physically unable to impinge on these regions as they will impact the nose and fuselage instead.

It is interesting that the concentration effect is still visible on the vertical tail. Because of the results near the wing root, one might logically assume that these particles are sufficiently massive enough to be considered purely ballistic. However, it is apparent from these results that the velocity gradient of the flow field still influences the trajectories of particles this massive.

This largest dropsize has the most significant water loading, with the exception of the engine that lies in the shadowzone. This case poses a significant icing risk, and it is apparent that the required anti-icing systems to protect against this dropsize would be extensive in nature.

Drop Size Distributions

Out of the six distributions tested, three share very similar water collection patterns. These three distributions are the "Langmuir D (20 μm)", "Freezing Drizzle MVD Less than 40 μm", and the "Freezing Rain MVD Less than 40 μm" distributions, and are pictured in Figures 14 to 16. None of these distributions led to collection efficiencies of one or greater suggesting that the icing risk is manageable. This is due to the fact that these three distributions contain roughly half of their water content at droplet diameters less than 20 μm, dropsizes that are very flow following.

There are significant variations between these three distributions with respect to the water content at larger dropsizes. These three distributions respectively contain roughly 1, 10, and 25 percent of their total water content at droplet diameters above 100 μm. This increase in water content at the larger dropsizes is reflected in the collection efficiency contours. There is increased impingement on the nose of the aircraft due to the ballistic nature of the water drops. There is also a decreased impingement on the engine cowling due to the cowling residing in the shadowzones of these large drops.
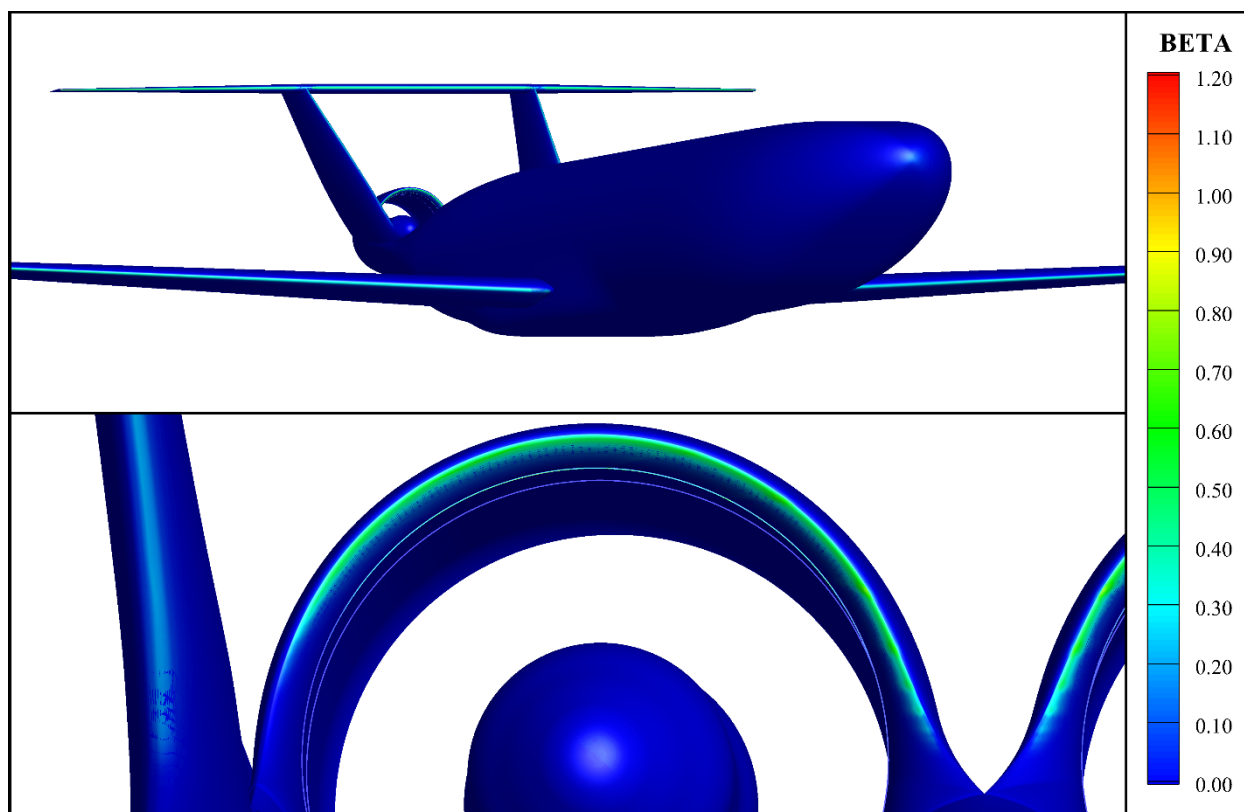
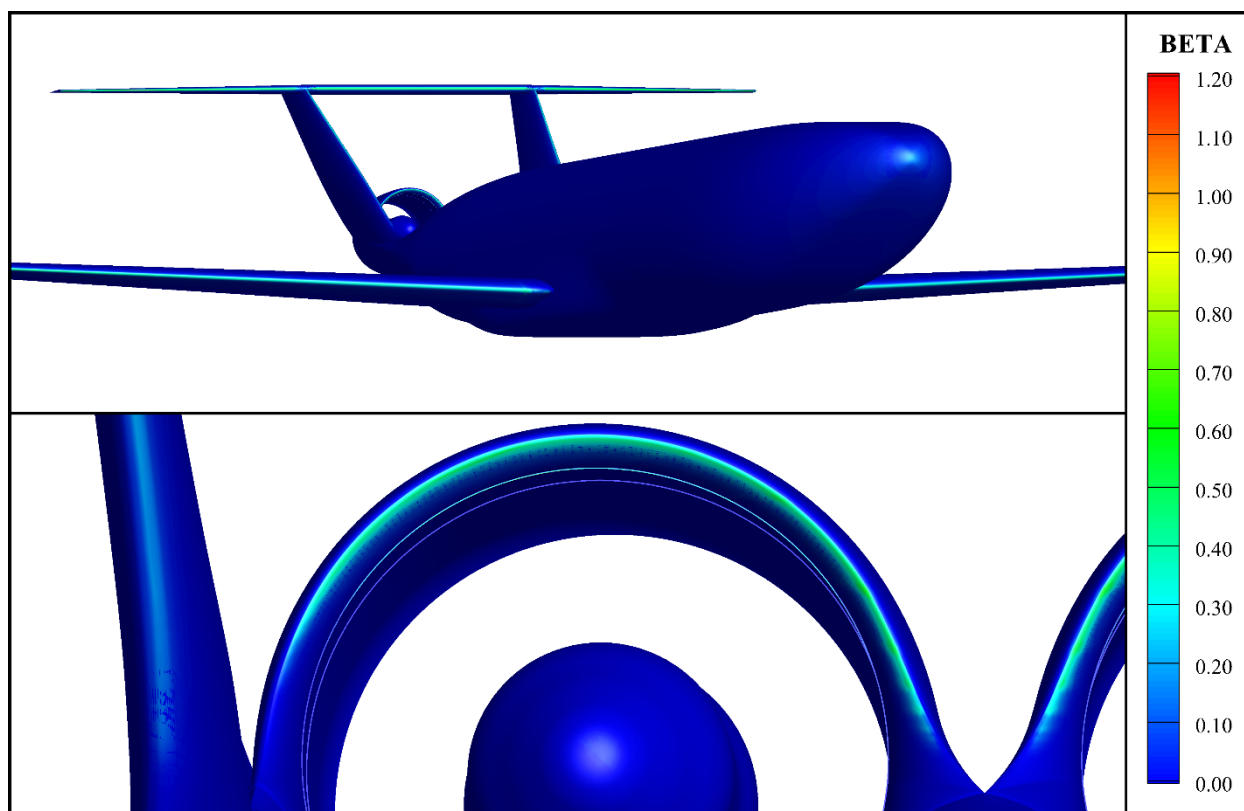Figure 14.—Collection Efficiencies for the Langmuir D 20 μm Distribution.

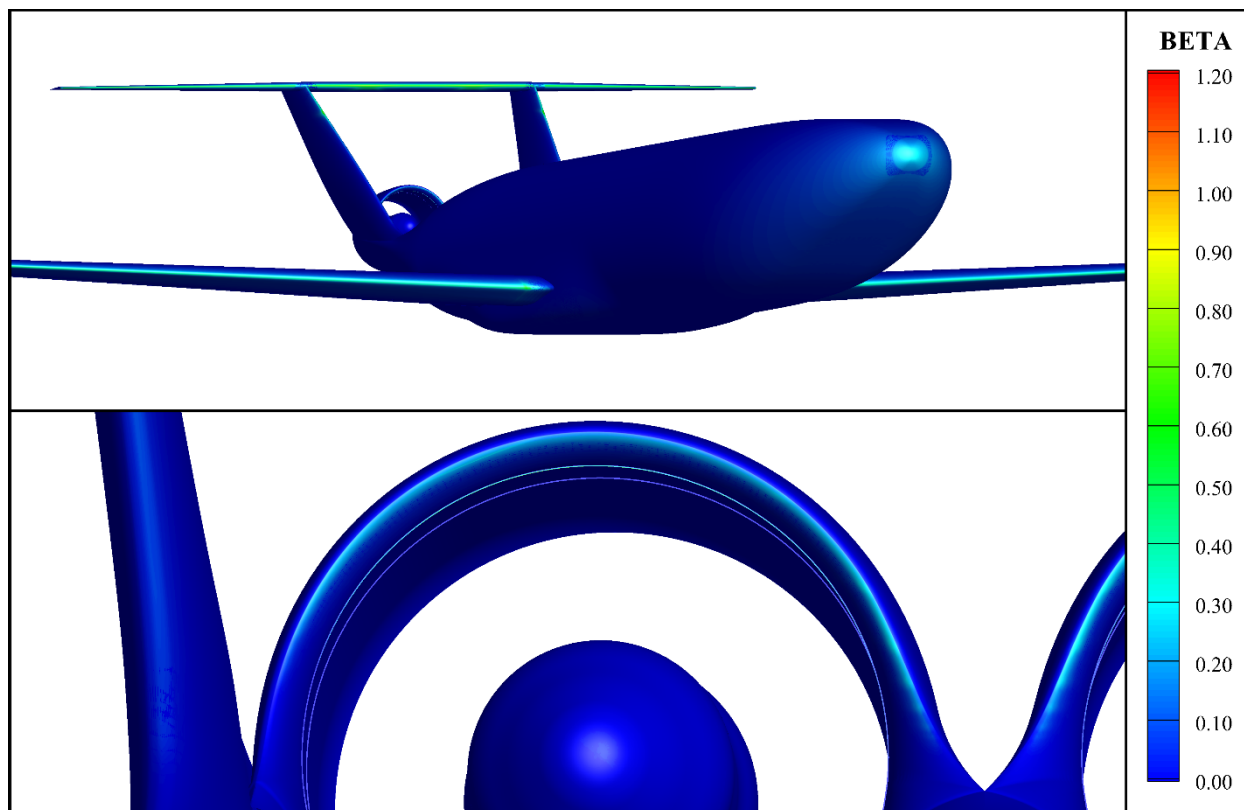Figure 15.—Collection Efficiencies for the Freezing Drizzle MVD Less than 40 μm Distribution.

Figure 16.—Collection Efficiencies for the Freezing Rain MVD Less than 40 µm Distribution.
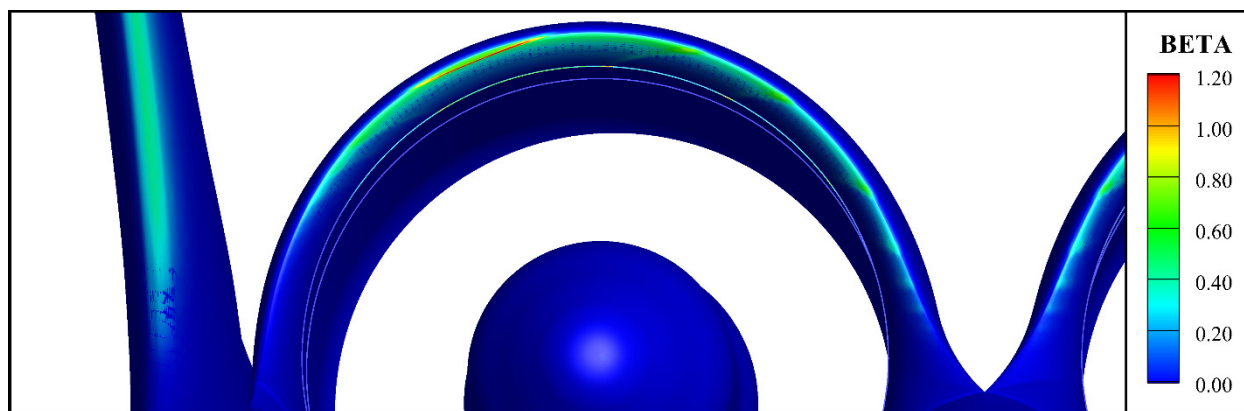

Figure 17.—Collection Efficiencies for the Langmuir D 40 µm Distribution.

The other three distributions are quite interesting. The Langmuir D (40 µm) distribution contains a significant amount of LWC at dropsizes that generate shadowzone boundaries on the engine cowling (i.e., dropsizes between 20 and 47 µm). Due to the discretization of the distribution, a striping effect can be seen on the cowling from the superposition of the concentration zones of high collection efficiency that border the shadowzone regions. This is pictured in Figure 17 and is a purely computational effect as a more resolved discretization of the droplet distribution would smooth out the discontinuities in this region. While the other distributions have water content at these dropsizes as well, it is not a sufficient fraction of the TWC to produce a striping effect as pronounced as the one associated with the Langmuir D (40 µm) distribution.

Even though this distribution contains the most water loading on the engine cowling, it is quite manageable when one disregards the striping due to the numerical discretization. Overall, collection efficiencies were low for the entire aircraft, and the threat of icing appears that it would be well managed with conventional anti-icing techniques.

The final two distributions are the Appendix O Freezing Drizzle and Freezing Rain MVD Greater than 40 μm distributions. These distributions contain a majority of their TWC at dropsizes greater than 100 μm, with the Freezing Rain distribution containing roughly 75 percent of its TWC over 100 μm with 15 percent over 1000 μm. The water collection patterns of these distributions can be seen in Figures 18 and 19.

The large amount of water in the SLD regime can significantly affect the solutions. Collection efficiencies on the leading edge of the wings and tails approach one, illustrating significant water loading and icing threat. The nose and underbody of the fuselage have impingement limits that extend much farther back than the Appendix C distributions, especially in the Freezing Rain condition, which poses a significant icing risk. These increases in water loading and impingement limits suggest that these Appendix O distributions will require more capable and extensive ice protection systems than those that protect against Appendix C conditions. Additionally, shadowzones and their neighboring concentration regions are also present on the wing near the fuselage as well as on the horizontal and vertical tails in the Freezing Rain condition.

The engine cowling for the large droplet cases received little water loading due to the lack of water content at the smaller dropsizes that impinge the cowling. It should be noted that these cases were run without a splashing model. Based on results from Reference 7, the splashing model would likely reduce the impingement limits on the nose and fuselage region of the aircraft. However, it would likely increase the water loading on the downstream regions where these splashed drops would reimpinge, such as the wing root region, tails, and perhaps even the engine cowling due to the large droplet breakup.
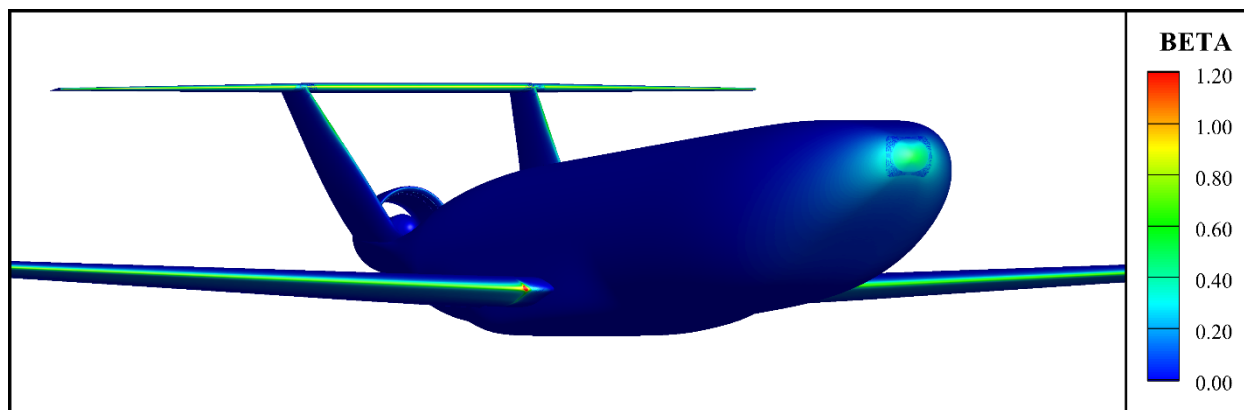

Figure 18.—Collection Efficiencies for the Freezing Drizzle MVD Greater than 40 μm Distribution.
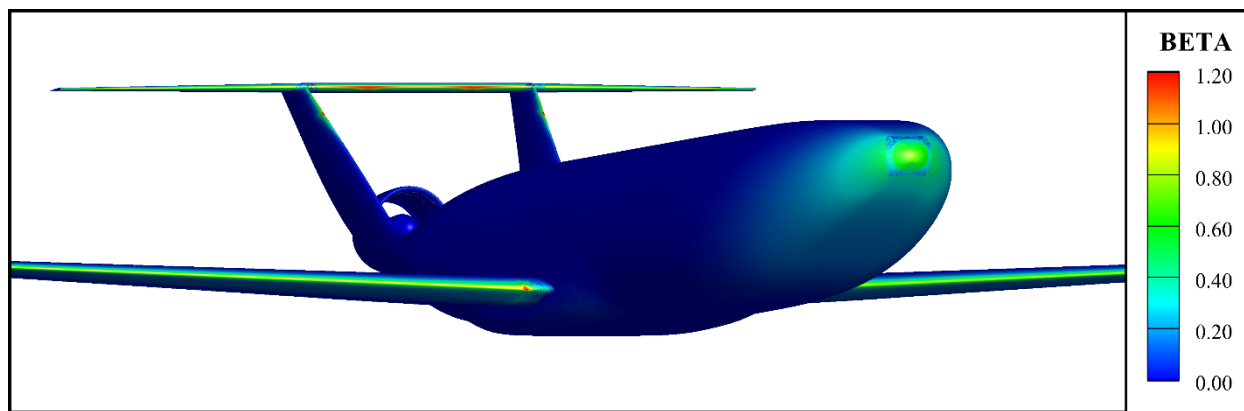

Figure 19.—Collection Efficiencies for the Freezing Rain MVD Greater than 40 μm Distribution.

More research, both computational and experimental, is needed to investigate the splashing phenomenon for this case. Reference 7 details comparisons of the splashing model for classical wing shapes subjected to impingement from moderately large drops. However, the D8 "Double Bubble" has a lifting nose component that is characterized by a large radius of curvature. In addition, the "Freezing Rain MVD Greater than 40 μm" distribution has roughly 60 percent of its water content at drop diameters larger than those tested in Reference 7. These unvalidated envelopes should be interrogated to ensure model accuracy, and extend conclusions from Reference 7 to these regimes.

Summary and Conclusions

CFD simulations of the D8 "Double Bubble" geometry from Overflow 2.2k were computed at NASA Ames Research Center and provided to the authors. These flow results were post processed with the use of LEWICE3D v3.63 to compute discrete droplet trajectories, surface impingement, and the resulting local collection efficiencies. For computational efficiency, droplet distributions were simulated by superposing weighted discrete droplet results from a 50-bin global distribution. This global distribution was projected onto the distributions of interest to determine the fractional water content contained in each bin for the various distributions. These fractions were used as weights in the superpositioning algorithm to compute the local collection efficiencies of the six distributions. The icing risk of the D8 "Double Bubble" aircraft was assessed by observing the water collection characteristics of these distributions from the Appendix C and O regimes. Since the amount of water collection correlates with resulting ice accretion size, potential performance impact, as well as anti-icing system requirements, this metric was utilized in this paper for the purposes of identifying icing risk. Therefore, regions of high collection efficiency were deemed to have a higher icing risk than regions of low or no collection efficiency.

With respect to infinite wing water droplet impingement, drop diameter variation typically only impacts the value of maximum collection efficiency and the impingement limits. The results here show that the flow field and droplet trajectories around a full wing body are much more complex. Significant variation in the shadowzone and neighboring concentration regions exist as a function of drop diameter. Due to the discrete nature of the droplet distributions, striping in the collection efficiency contours can occur as a result of the superposition of the step changes of collection efficiency in these regions. This striping would diminish into a fully smooth contour as the amount of bins discretely representing the distribution goes to infinity.

The distribution that posed the highest risk for ice accretion on the engine cowling was the Langmuir D (40 μm) distribution. This is due to the fact that this distribution contained significant amounts of water in dropsizes that produced the highest water impingement on the engine cowling surface (i.e., 20 to 47 μm). Even though this case contains the most water loading on the engine cowling, collection efficiencies weren't that high when one disregards the striping that occurs due to the numerical discretization, and the overall icing risk of this distribution is manageable.

The distributions with the largest dropsizes correlated with the largest water loading and impingement limits, as well as exhibiting regions of collection efficiencies that exceed unity. These large dropsize distributions are from the Appendix O regime that future aircraft must comply with. When one compares the water loading of these distributions to the Appendix C distributions, it becomes quite evident that significant increases in ice protection capability are likely necessary to navigate through these Appendix O regimes.

The simulations did not make use of the splashing model in LEWICE3D. Based on prior results from Reference 7, this would have likely resulted in reduced impingement limits for the large dropsize cases, as well as increasing water loading on downstream geometry such as wing root region, tails, and perhaps even the engine cowling due to the large droplet breakup. The impact of the splashing model on the simulations requires further investigation, with specific interest centering around the susceptibility of the engine cowling to water loading for the large droplet cases. This effort would require experimental validation, as it is unclear whether SLD of differing orders of magnitude (e.g., 100 vs. 1000 μm) on differing geometries (e.g., classical wings vs. large radius of curvature lifting fuselages) splash in similar fashions.

Appendix—Comprehensive Contour Plots

For the benefit of the reader, comprehensive contour plots of the four discrete and six distribution simulations are contained in this appendix. It should be noted that many of the subplots have been included in the Results and Discussion portion of this paper, however including all of them was not necessary and would have impacted the readability of the paper. Each figure consists of four subplots which highlight the surface contours of four different regions of the aircraft. The four different views presented in the subplots from top to bottom are:

1. A nearly complete view of the entire aircraft highlighting water collection on the nose and fuselage of the aircraft, while also giving some global perspective of the other three subplots.
2. A zoomed in view highlighting water collection on the vertical and horizontal tails.
3. A zoomed in view highlighting water collection on the cowling of the engine inlet.
4. A zoomed in view highlighting water collection on the leading edge of the wing near the root.
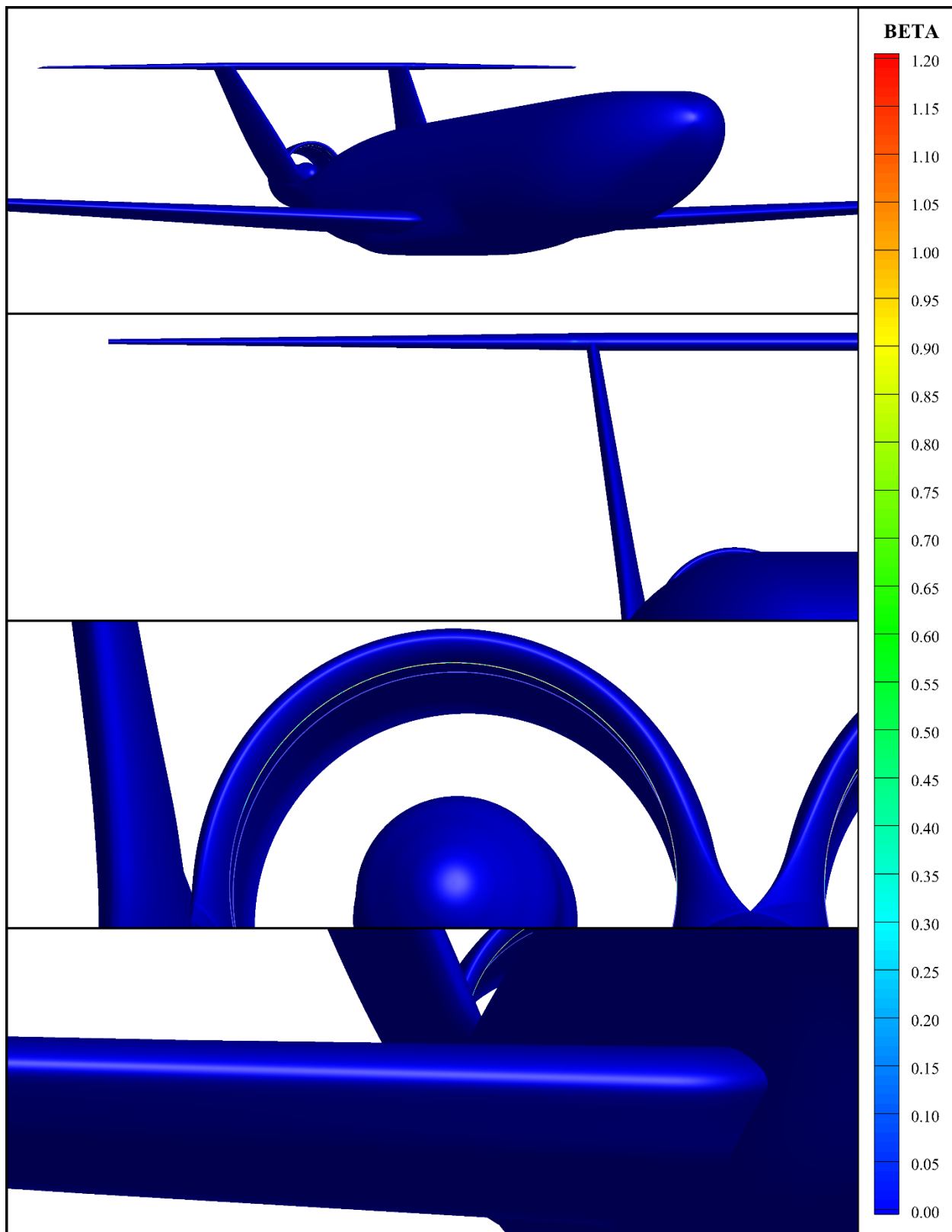
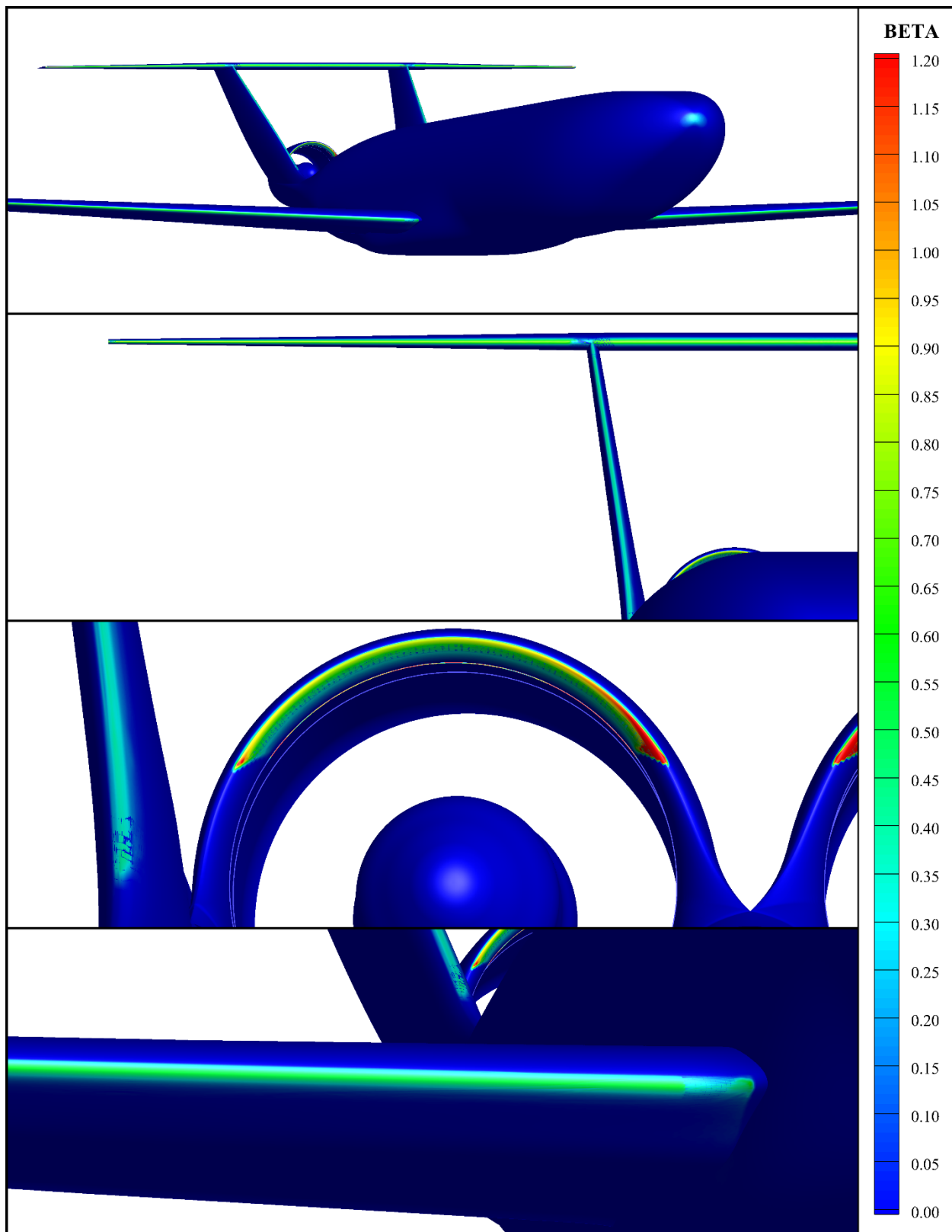Figure 20.—Collections Efficiencies for Bin 1, a Discrete Drop Diameter of 5 µm.

Figure 21.—Collection Efficiencies for Bin 17, a Discrete Drop Diameter of 33 μm.
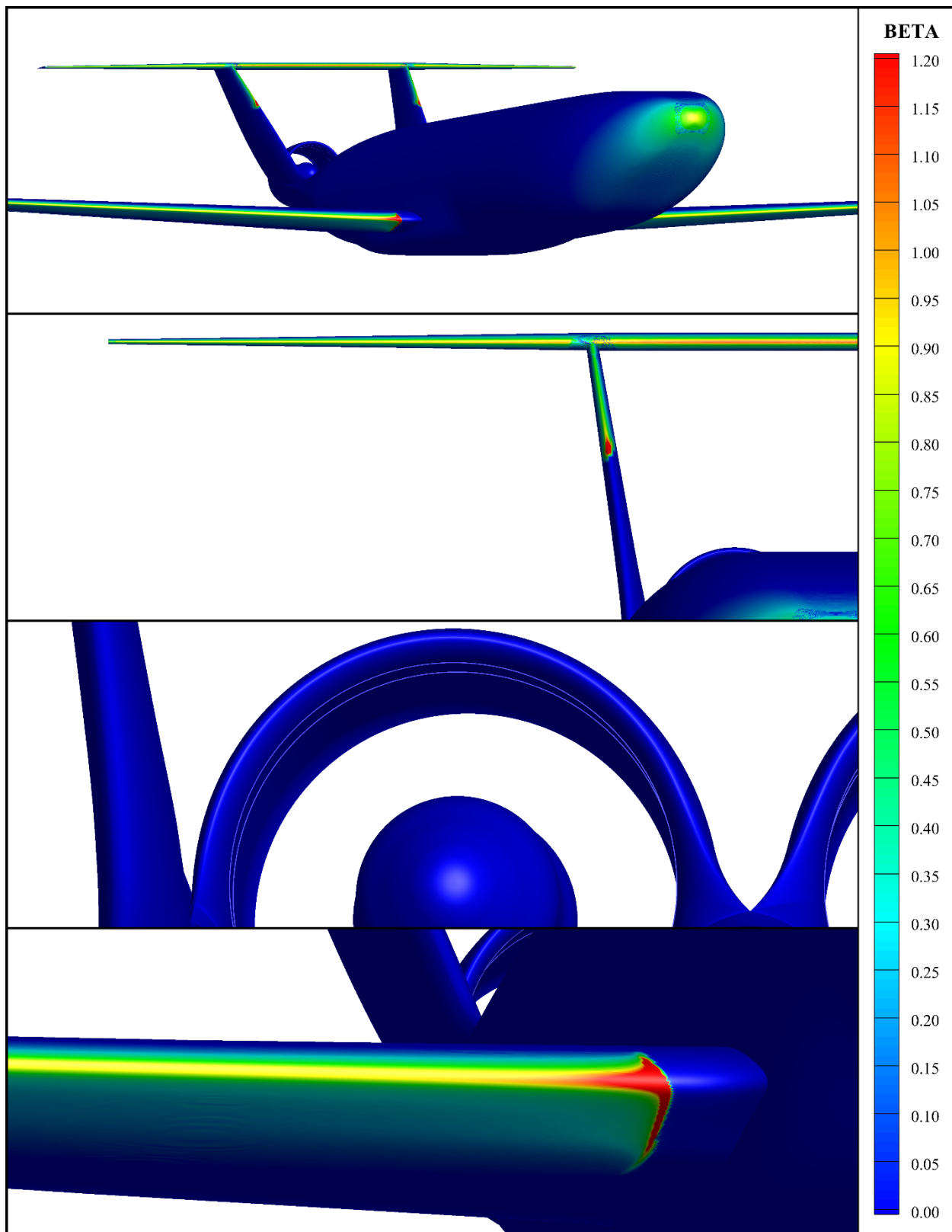
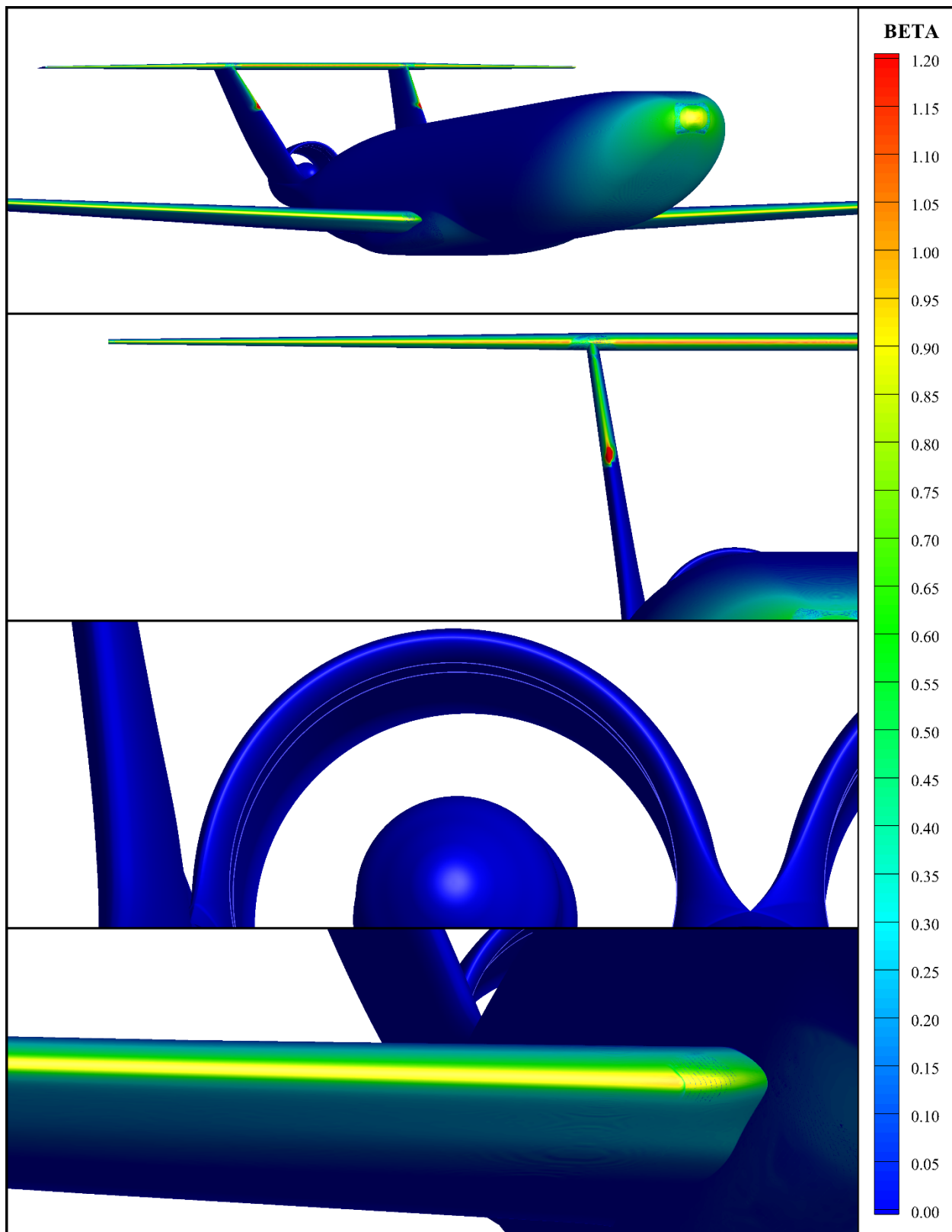Figure 22.—Collection Efficiencies for Bin 34, a Discrete Drop Diameter of 244 µm.

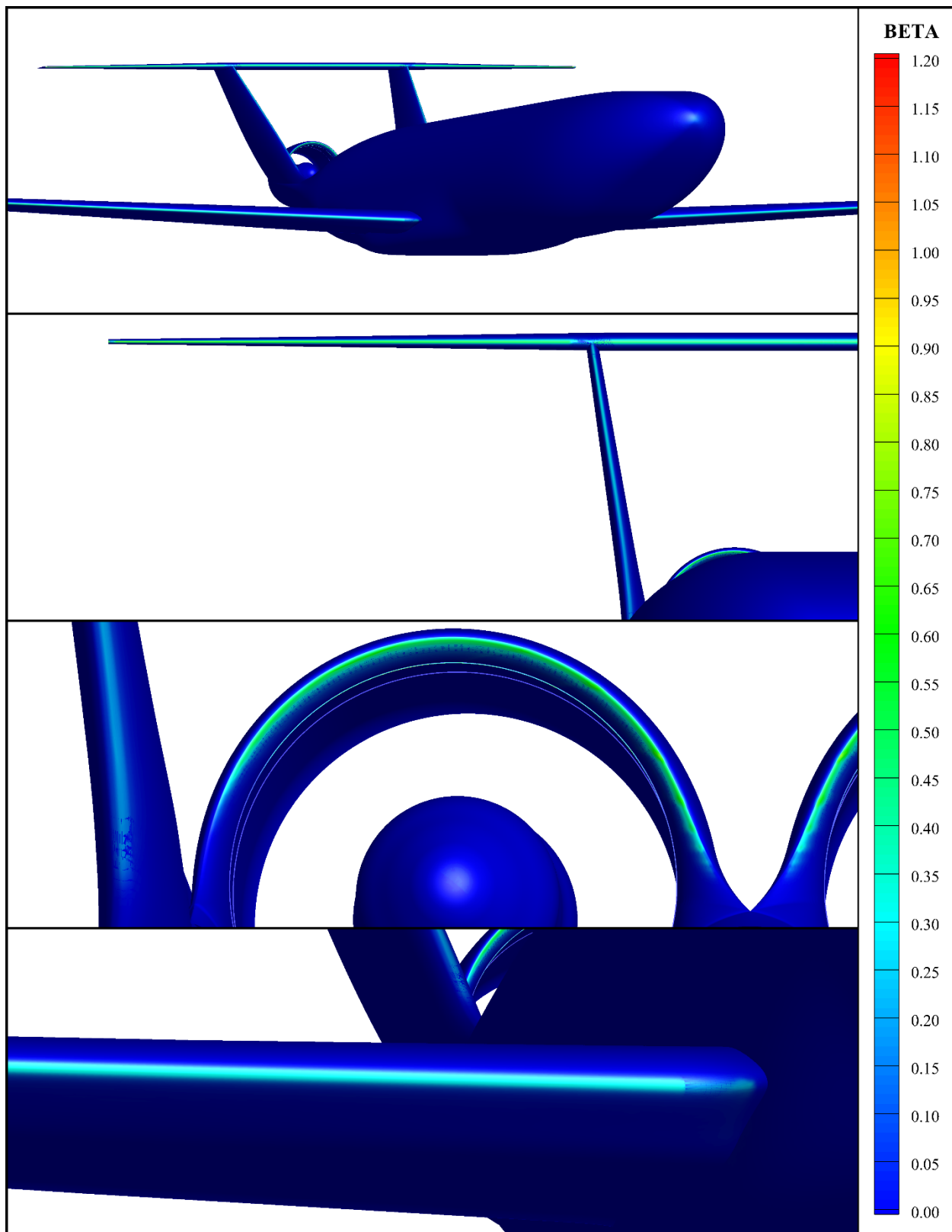Figure 23.—Collection Efficiencies for Bin 50, a Discrete Drop Diameter of 1605 µm.

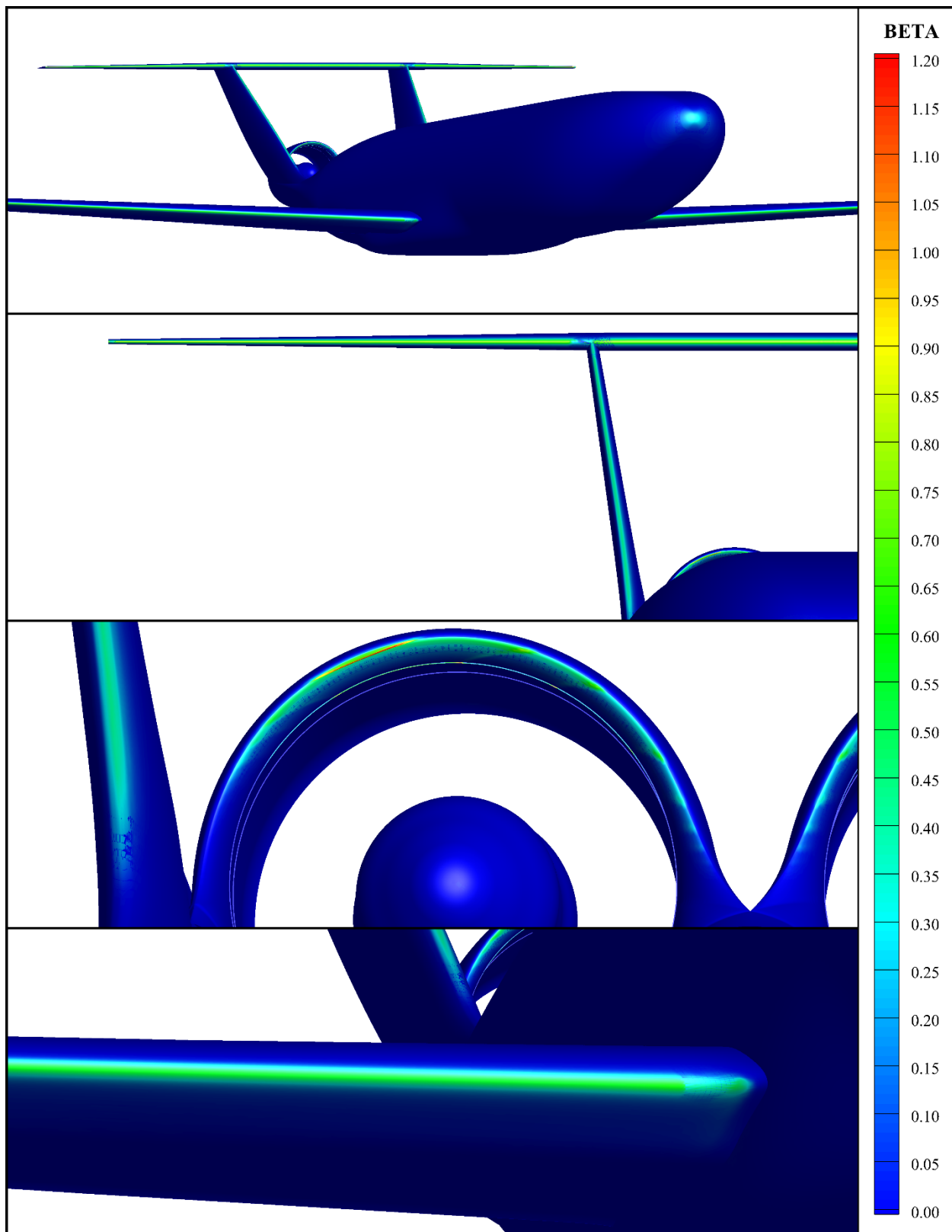Figure 24.—Collection Efficiencies for the Langmuir D 20 μm Distribution.

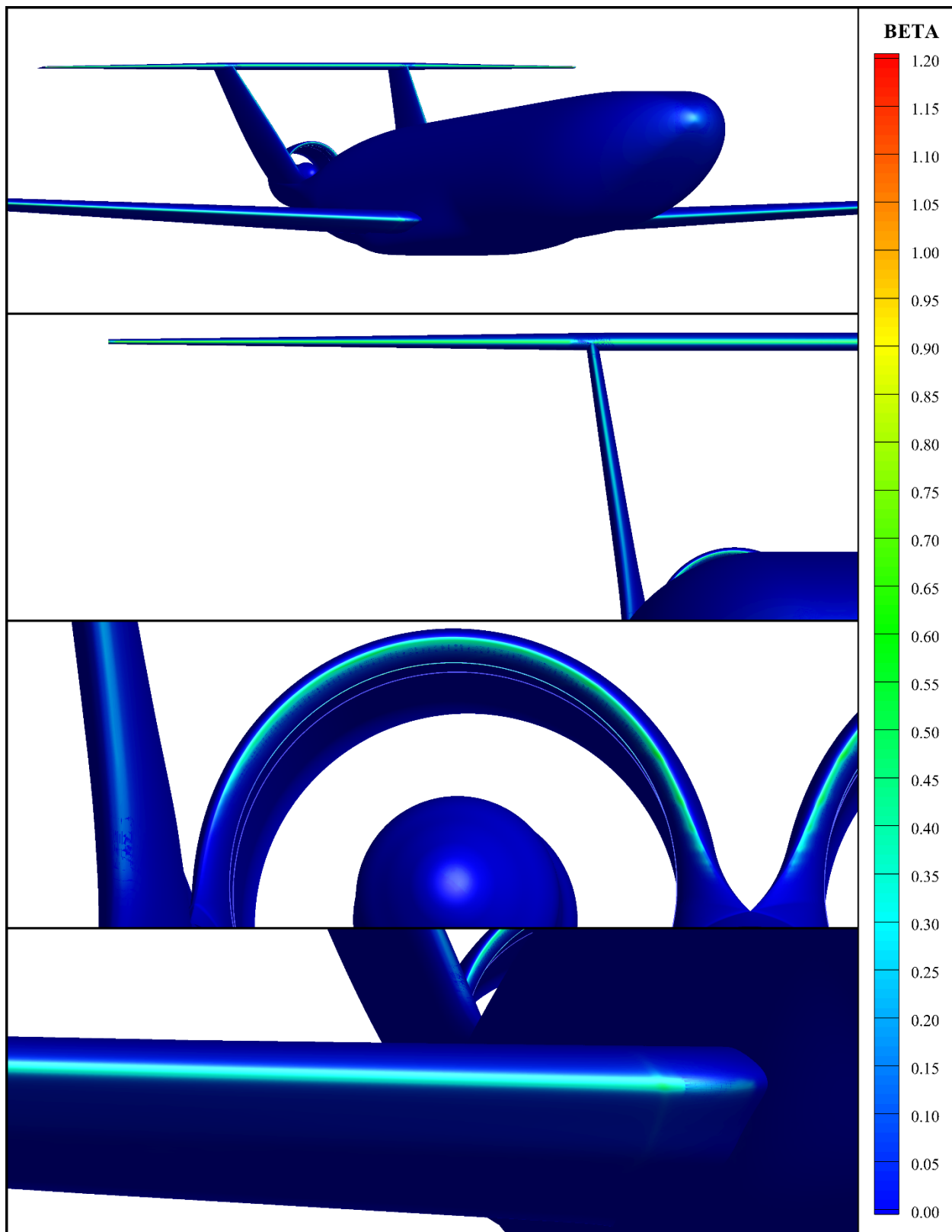Figure 25.—Collection Efficiencies for the Langmuir D 40 µm Distribution.

Figure 26.—Collection Efficiencies for the Freezing Drizzle MVD Less than 40 μm Distribution.
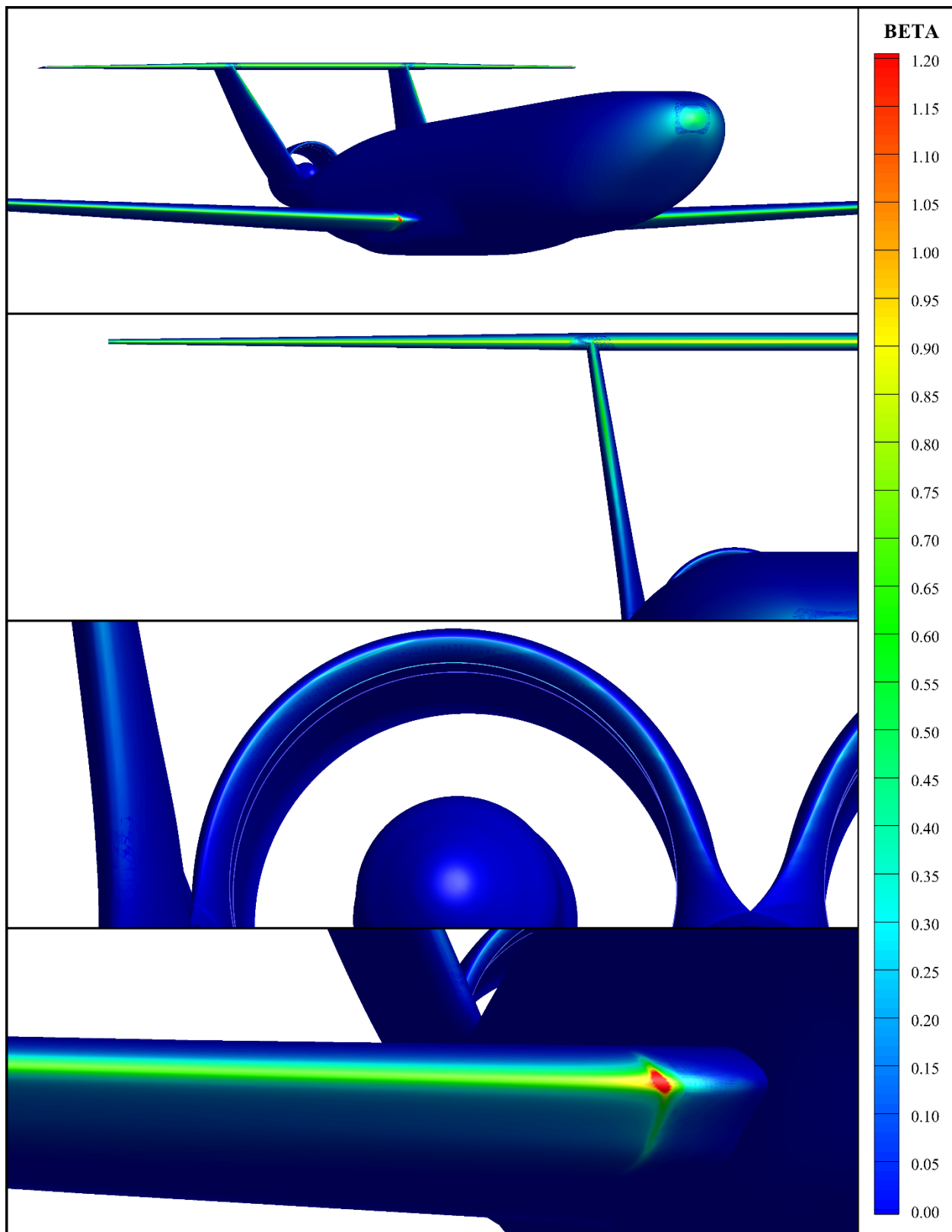
Figure 27.—Collection Efficiencies for the Freezing Drizzle MVD Greater than 40 µm Distribution.
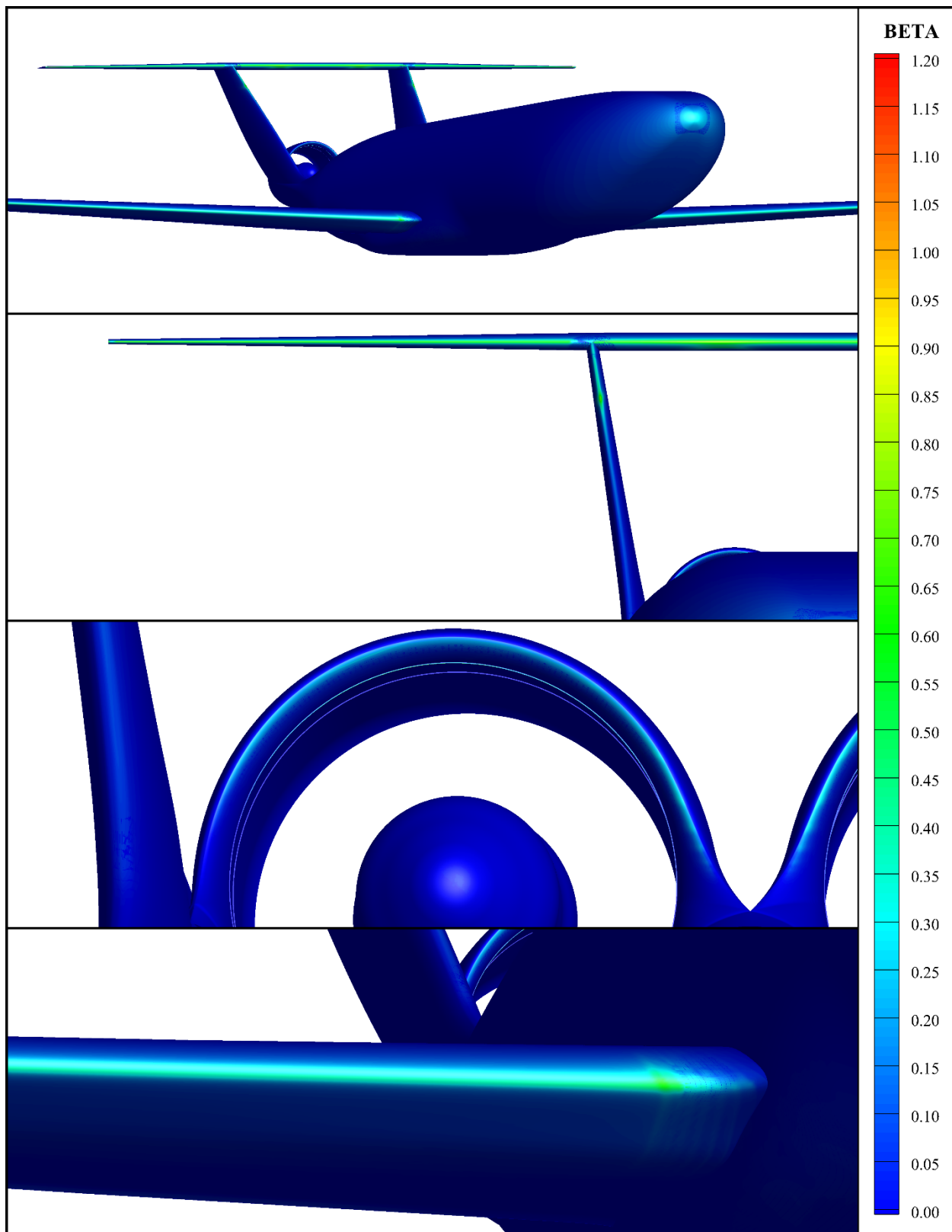
Figure 28.—Collection Efficiencies for the Freezing Rain MVD Less than 40 µm Distribution.
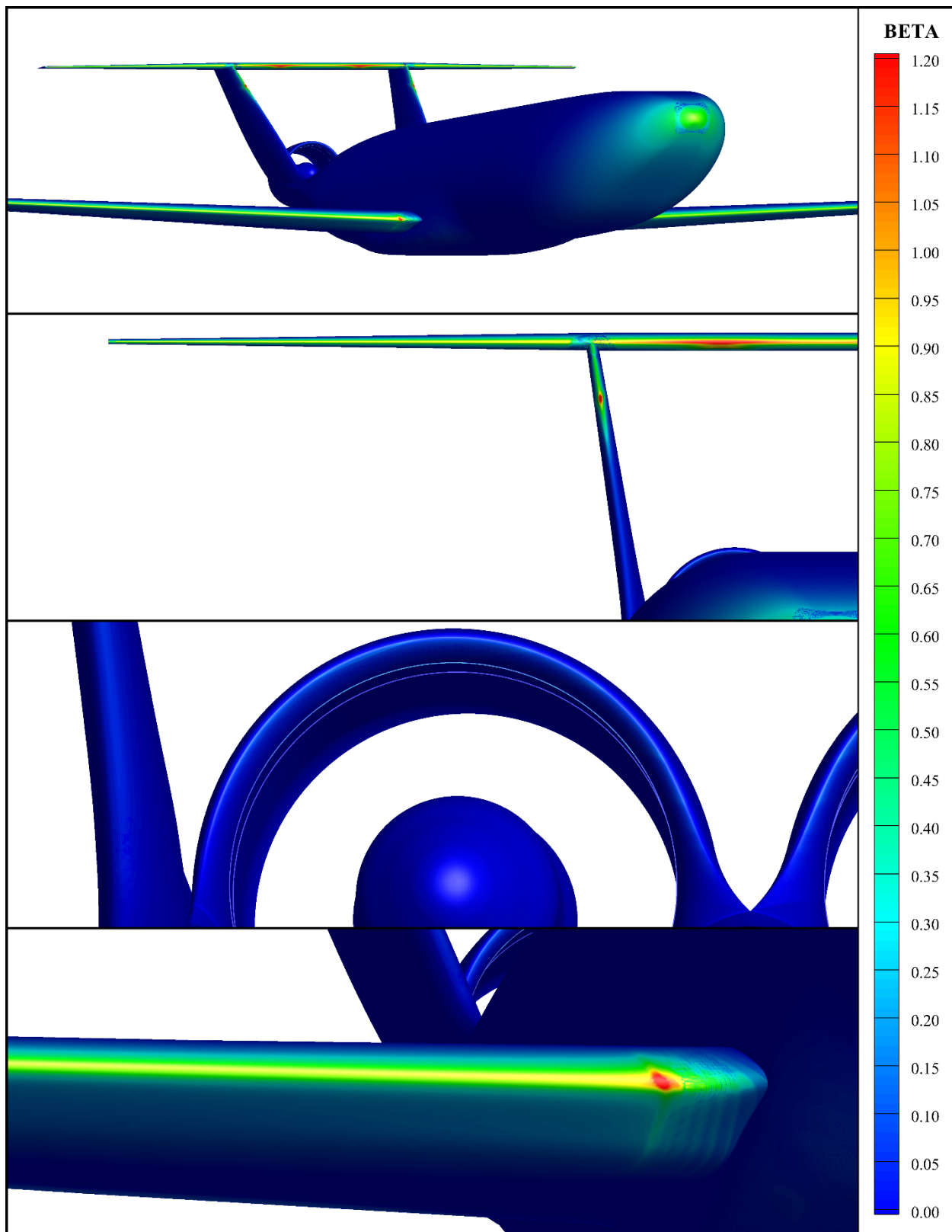
Figure 29.—Collection Efficiencies for the Freezing Rain MVD Greater than 40 μm Distribution.

References

1. Del Rosario, R., et al. "Subsonic Fixed Wing Project Overview of Technical Challenges for Energy Efficient, Environmentally Compatible Subsonic Transport Aircraft." *50th AIAA Aerospace Science Meeting, Nashville, TN* (2012).
2. Bidwell, Colin S. "User's Manual for the NASA Glenn Three-Dimensional Grid Based Ice Accretion Code (LEWI3DGR Ver. 1.7)." (2005).
3. Wright, William B. "User Manual for the NASA Glenn Ice Accretion Code LEWICE. Version 2.2.2." (2002).
4. Title 14 Code of Federal Regulations, Aeronautics and Space, Part 25 Airworthiness Standards: Transport Category Airplanes, Section C25.1: Appendix C; published by the Office of the Federal Register, National Archives and Records Administration, Washington, DC., Amdt. 25-140, effective 5-Jan-2015
5. Title 14 Code of Federal Regulations, Aeronautics and Space, Part 25 Airworthiness Standards: Transport Category Airplanes, Section O25.1: Appendix O; published by the Office of the Federal Register, National Archives and Records Administration, Washington, DC., Amdt. 25-140, effective 5-Jan-2015.
6. Bidwell, Colin S. "Icing Analysis of a Swept NACA 0012 Wing Using LEWICE3D Version 3.48." *AIAA Aviation Forum, Atlanta, GA* (2014).
7. Bidwell, Colin S. "Super Cooled Large Droplet Analysis of Several Geometries Using LEWICE3D Version 3." *AIAA Atmospheric and Space Environments Conference, Toronto, ON* (2010).
8. Papadakis, Michael, et al. "Comparison of Experimental and Computational Ice Shapes for an Engine Inlet." *AIAA Atmospheric and Space Environments Conference, Toronto, ON* (2010).
9. Bidwell, Colin S. "Icing Calculations for a 3D, High-Lift Wing Configuration." *43rd AIAA Aerospace Sciences Meeting and Exhibit, Reno, NV* (2005).
10. Bidwell, Colin. "Icing Analysis of the NASA S3 Icing Research Aircraft Using LEWICE3D Version 2." No. 2007-01-3324. SAE Technical Paper, 2007.
11. Greitzer, Edward M., et al. "N+3 Aircraft Concept Designs and Trade Studies, Final Report." *NASA/CR—2010-216794/Vol.1* (2010).
12. Nichols, Robert H., and Peter G. Buning. "User's Manual for OVERFLOW 2.2." *University of Alabama and NASA Langley Research Center* (2015).
13. Menter, F. "Zonal Two Equation κ-ω Turbulence Models for Aerodynamic Flows." *24th AIAA Fluid Dynamics Conference, Orlando, FL* (1993).
14. Langmuir, Irving, and Katherine Blodgett. "Mathematical Investigation of Water Droplet Trajectories." *AAFTR 5418* (1946).
15. Heinrich, A., et al. "Aircraft Icing Handbook, Volume I." *DOT/FAA/CT-88/8-1* (1991).
16. Papadakis, Michael, et al. "Large and Small Droplet Impingement Data on Airfoils and Two Simulated Ice Shapes." *NASA/TM—2007-213959* (2007).